Anisotropic scattering effects of a gyrotropic sphere characterized using the T-matrix method

Joshua Le-Wei Li
Institute of Electromagnetics and School of Electronic Engineering, University of Electronic Science and Technology of China, Chengdu, China 611731

Wee-Ling Ong and Katherine H. R. Zheng
Department of Electrical and Computer Engineering, National University of Singapore, Kent Ridge, Singapore 119260
(Received 19 July 2011; published 5 March 2012)

Solutions for characterizing both electromagnetic wave propagation in, and scattering by, a gyrotropic sphere are obtained based on some recently published literature. Both gyrotropic permittivity and permeability tensors are considered herein, and both transmitted internal fields and scattered external fields are derived theoretically. Compared with problems of a uniaxial sphere, a gyroelectric sphere, and a gyromagnetic sphere, the scattering problem considered here is found to be astonishingly complicated but more generalized in formulation and solution procedure. Numerical validations are made by reducing our results to a gyromagnetic sphere and comparing them with the results obtained using the Fourier transform method, where excellent agreements are observed. Then, radar cross sections (RCSs) versus electric and magnetic gyrotropy ratios are computed, while hybrid effects due to both electric and magnetic gyrotropies are studied extensively, where some special cases of uniaxial spheres are demonstrated. It is shown that characteristics of gyrotropy parameters in Cartesian coordinates may lead to considerably large variations in RCS values, elucidating physical significance of gyrotropy and anisotropy ratios in scattering control. The *generalized* formulation of the problem is expected to have *wide practical* applications, while some features of this gyrotropic sphere may help other researchers or engineers to understand more physical insight. In addition, some critical mistakes made in literature were corrected.

DOI: 10.1103/PhysRevE.85.036601 PACS number(s): 03.50.De, 81.05.Xj, 41.20.−q, 42.25.Fx

I. INTRODUCTION

Scattering by anisotropic spheres or spheres of anisotropic media has attracted continued interests of both physics and engineering communities over the last several decades [1–13], and research interests were extended from geophysics, nuclear physics, quantum effects, nanoparticles, photonic crystals, and dielectric materials associated with gravitational, elastic, acoustic, electromagnetic, and/or light waves. Electromagnetic characterization of anisotropic media has been a focused research topic [4,6,8,11,14–17] due to easy realizations of artificial composites such as magnetically biased ferrite or plasma, for instance, gyrotropic materials, which are also known as nonreciprocal anisotropic media. By nonreciprocity, it means that the gyrotropic materials are sensitive to the direction of waves propagating inside the materials [2,18]. This nonreciprocal behavior is due to a reorientation of the eigenaxes between forward and backward transit [19]. Under time reversal, gyrotropic processes are fully reciprocal. It flips both the propagation direction and electron spin, which is the source of magnetization.

Over the past many years, various numerical and analytical methods have been reported and utilized to characterize interactions between electromagnetic waves and anisotropic media in general, for instance, the method of moments (MoM) [20], the transmission line modeling [18], the coupled dipole approximation method [21], the integral equation method [22], the spectral domain Fourier transformation approach [23,24], and the mode expansion method [25,26].

The magnetic and electric uniaxial spheres as well as the gyroelectric spheres (the permittivity and permeability tensors of which are often expressed in Cartesian coordinates system) have been studied extensively by Geng *et al.* [27–30]. Geng *et al.* have employed the spherical vector wave function expansion method together with the Fourier transform technique to derive the analytical solutions for the plane wave scattering by a plasma anisotropic sphere [27], a uniaxial anisotropic sphere [28], a multilayer plasma anisotropic sphere [29], and an impedance sphere coated with a uniaxial anisotropic layer [30]. In addition, Lin *et al.* [31] have obtained a solution for a gyromagnetic sphere using the multiple scattering method along with the T-matrix method. Subsequently, this method was adopted by a few researchers to investigate the scattering problem by a single electric uniaxial sphere [32–35]. In addition to the above anisotropy form of the materials described in the Cartesian coordinates system, Liu *et al.* [36] and Qiu *et al.* have investigated characteristics of electromagnetic waves for radial uniaxial and gyrotropic spheres, the permittivity and permeability tensors of which are expressed in the spherical coordinates system [37–41] for realizing the classical spherical cloaking. According to Gao *et al.* [26], the radius ratios of radial anisotropy coated spheres can be adjusted so as to make objects nearly "transparent" or "invisible."

Both gyrotropic permittivity $\overline{\epsilon}$ and permeability $\overline{\mu}$ tensors were considered for the cylindrical case [42] and the radial anisotropic sphere [37,43] to have a better physical insight into the problem. There are, however, no general solutions for electromagnetic or light scattering by a sphere, the gyrotropic tensors of which are expressed in the Cartesian coordinates system. Herein, we thus consider the multiple scattering method together with the T-matrix method to obtain

a generalized solution of electromagnetic scattering by a sphere which has a hybrid gyrotropic property. As both gyrotropic permittivity and permeability tensors are considered, the formulations carried out herewith based on the vector eigenfunction expansions are physically more generalized and mathematically astonishingly complicated; meanwhile, the theoretical derivations and numerical calculations are also very tedious and much involved, making the problem far more difficult than those previous works in literature. In addition, the procedure can be applied to arbitrary polarizations of the incident waves, which makes the detailed formulations necessarily general enough for many different kinds of practical applications. After the analytical solution to the problem defined is obtained, we also present some numerical results for the physical insights into the scattering problem. We validate our derived formulation and developed codes by reducing our results to simpler cases of a gyromagnetic sphere and then by comparing the results obtained using our approach and the Fourier transform method. As shown later, a very good agreement is observed for both trials. In addition, we have considered a number of examples and obtained many different sets of the results. Associated with these results, various physical insights resulted in by the nature of the problem are discussed, and different kinds of hybrid effects of scattering geometry and electrical parameters are summarized. The results inside the paper provide some mathematical formulations and also some important physical insights, both with good potential physical and engineering applications in the near future.

II. BASIC FORMULAS

A. Expansion of electromagnetic field inside the sphere

In the subsequent analysis, a time dependence of the form $e^{-i\omega t}$ is assumed and will be suppressed throughout the treatment. Consider an anisotropic sphere in free space with a radius of a and its center located at spherical coordinates origin, as shown in Fig. 1.

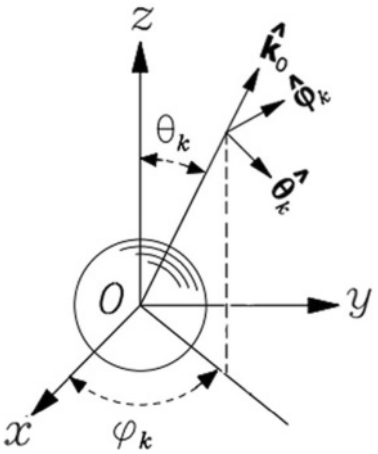

FIG. 1. Geometry for electromagnetic scattering of plane wave by an anisotropic sphere in free space.

The sphere is characterized by a permeability tensor and a permittivity tensor of the forms

$$\overline{\boldsymbol{\mu}} = \mu_s \begin{bmatrix} \mu_t & -i\mu_g & 0 \\ i\mu_g & \mu_t & 0 \\ 0 & 0 & 1 \end{bmatrix}, \tag{1a}$$

$$\overline{\boldsymbol{\epsilon}} = \epsilon_s \begin{bmatrix} \epsilon_t & -i\epsilon_g & 0 \\ i\epsilon_g & \epsilon_t & 0 \\ 0 & 0 & 1 \end{bmatrix}. \tag{1b}$$

So, the following constitutive relations inside the sphere are thus considered:

$$\boldsymbol{D}_{\text{int}} = \overline{\boldsymbol{\epsilon}} \cdot \boldsymbol{E}_{\text{int}}, \tag{2a}$$

$$\boldsymbol{B}_{\text{int}} = \overline{\boldsymbol{\mu}} \cdot \boldsymbol{H}_{\text{int}}. \tag{2b}$$

From the source-free Maxwell's equations, we obtain

$$\nabla \times \left[\epsilon_s \overline{\boldsymbol{\epsilon}}^{-1} \cdot (\nabla \times \mu_s \overline{\boldsymbol{\mu}}^{-1} \cdot \boldsymbol{B}_{\text{int}})\right] - k_s^2 \boldsymbol{B}_{\text{int}} = 0, \tag{3}$$

where $k_s^2 = \omega^2 \epsilon_s \mu_s$. The two inverse matrices are explicitly expressed as

$$\mu_s \overline{\boldsymbol{\mu}}^{-1} = \begin{bmatrix} \mu_t' & -i\mu_g' & 0 \\ i\mu_g' & \mu_t' & 0 \\ 0 & 0 & 1 \end{bmatrix}, \tag{4a}$$

$$\epsilon_s \overline{\boldsymbol{\epsilon}}^{-1} = \begin{bmatrix} \epsilon_t' & -i\epsilon_g' & 0 \\ i\epsilon_g' & \epsilon_t' & 0 \\ 0 & 0 & 1 \end{bmatrix}, \tag{4b}$$

where

$$\mu_t' = \frac{\mu_t}{\mu_t^2 - \mu_g^2}, \tag{5a}$$

$$\mu_g' = -\frac{\mu_g}{\mu_t^2 - \mu_g^2}, \tag{5b}$$

$$\epsilon_t' = \frac{\epsilon_t}{\epsilon_t^2 - \epsilon_g^2}, \tag{5c}$$

$$\epsilon_g' = -\frac{\epsilon_g}{\epsilon_t^2 - \epsilon_g^2}. \tag{5d}$$

Since $\nabla \cdot \boldsymbol{B}_{\text{int}} = 0$, we can express the magnetic flux density inside the sphere as

$$\boldsymbol{B}_{\text{int}} = \sum_{n,m} \overline{E}_{mn} \left[d_{mn} \boldsymbol{M}_{mn}^{(1)}(k,\boldsymbol{r}) + c_{mn} \boldsymbol{N}_{mn}^{(1)}(k,\boldsymbol{r})\right], \tag{6}$$

where k denotes the wave number yet to be determined, while the $\boldsymbol{M}_{mn}^{(1)}(k,\boldsymbol{r})$ and $\boldsymbol{N}_{mn}^{(1)}(k,\boldsymbol{r})$ stand for the first kind of spherical vector wave functions of transverse electric (TE) and transverse magnetic (TM) modes. The summation coefficient is defined as $\overline{E}_{mn} = i^n E_0 C_{mn}$ where C_{mn} is given by [44,45]

$$C_{mn} = \left[\frac{2n+1}{n(n+1)} \frac{(n-m)!}{(n+m)!}\right]^{\frac{1}{2}}, \tag{7}$$

while E_0 represents the amplitude of the incident electric field. Unless explicitly specified, hereinafter the summation $\sum_{m,n}$ implies the n runs from 1 to $+\infty$, and m from $-n$ to n for each n. In practical calculations, the expansion is supposed to be uniformly convergent and can be truncated approximately at $n = n_c = x + 4x^{1/3} + 2$ [46,47], where $x = k_0 a$ with k_0 and a being the free space wave number and the radius of the sphere,

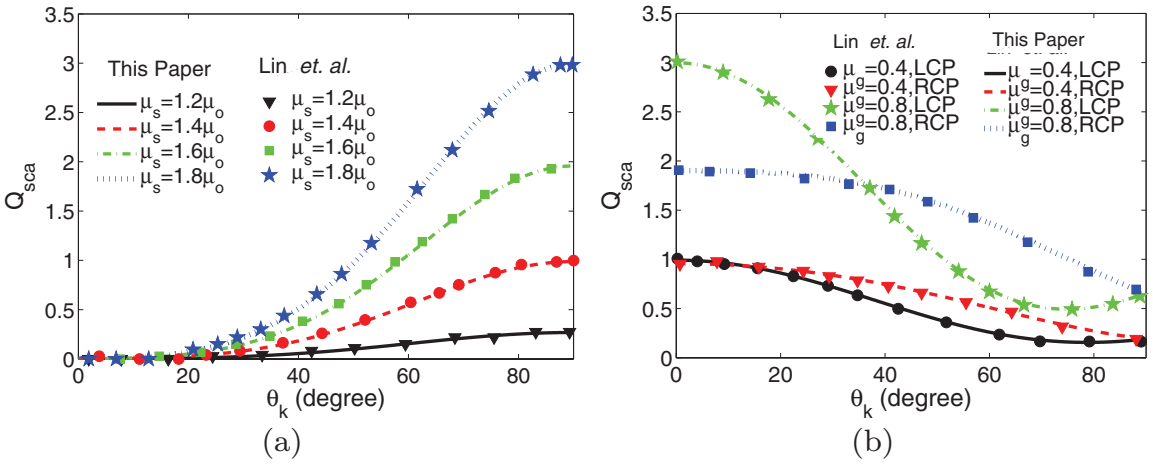

FIG. 2. (Color online) $Q_{\rm sca}$ versus incident angle θ_k for (a) $\mu_g = 0$ and $\mu_s\mu_t = \mu_0$ at various values of μ_s. The polarizations are assumed to be $(p_\theta, p_\phi) = (0,1)$ and $x = 4.25$. (b) $x = 4.0$, $\mu_s = \mu_0$, and $\mu_t = 1$ at various values of μ_g. LCP and RCP represent the left- and right-handed circularly polarized incident waves with $(p_\theta, p_\phi) = 1/\sqrt{2}(1, i)$ and $1/\sqrt{2}(1, -i)$, respectively.

respectively.[1] Although this function was developed for the isotropic case where the relative permittivity and permeability of the sphere are not related, it was found that this function is still valid for the anisotropic media in a relaxed way [35].

With the use of the properties of spherical vector wave functions, it can be worked out that

$$\mu_s\overline{\boldsymbol{\mu}}^{-1}\cdot\boldsymbol{M}_{uv} = \sum_{q=0}^{+\infty}\sum_{p=-q}^{+q}\left[\tilde{g}_{pq}^{uv}\boldsymbol{M}_{pq} + \tilde{e}_{pq}^{uv}\boldsymbol{N}_{pq} + \tilde{f}_{pq}^{uv}\boldsymbol{L}_{pq}\right], \tag{8a}$$

$$\mu_s\overline{\boldsymbol{\mu}}^{-1}\cdot\boldsymbol{N}_{uv} = \sum_{q=0}^{+\infty}\sum_{p=-q}^{+q}\left[\overline{g}_{pq}^{uv}\boldsymbol{M}_{pq} + \overline{e}_{pq}^{uv}\boldsymbol{N}_{pq} + \overline{f}_{pq}^{uv}\boldsymbol{L}_{pq}\right], \tag{8b}$$

$$\epsilon_s\overline{\boldsymbol{\epsilon}}^{-1}\cdot\boldsymbol{M}_{mn} = \sum_{q=0}^{+\infty}\sum_{p=-q}^{+q}\left[\tilde{o}_{pq}^{mn}\boldsymbol{M}_{pq} + \tilde{p}_{pq}^{mn}\boldsymbol{N}_{pq} + \tilde{q}_{pq}^{mn}\boldsymbol{L}_{pq}\right], \tag{8c}$$

$$\epsilon_s\overline{\boldsymbol{\epsilon}}^{-1}\cdot\boldsymbol{N}_{mn} = \sum_{q=0}^{+\infty}\sum_{p=-q}^{+q}\left[\overline{o}_{pq}^{mn}\boldsymbol{M}_{pq} + \overline{p}_{pq}^{mn}\boldsymbol{N}_{pq} + \overline{q}_{pq}^{mn}\boldsymbol{L}_{pq}\right], \tag{8d}$$

where the coefficients $\tilde{g}_{pq}^{uv}$, $\tilde{e}_{pq}^{uv}$, $\tilde{f}_{pq}^{uv}$, $\tilde{o}_{pq}^{mn}$, $\tilde{p}_{pq}^{mn}$, $\tilde{q}_{pq}^{mn}$, $\overline{g}_{pq}^{uv}$, $\overline{e}_{pq}^{uv}$, $\overline{f}_{pq}^{uv}$, $\overline{o}_{pq}^{mn}$, $\overline{p}_{pq}^{mn}$, and $\overline{q}_{pq}^{mn}$ are given in the Appendix. Therefore, we have

$$\mu_s\overline{\boldsymbol{\mu}}^{-1}\cdot\boldsymbol{B}_{\rm int} = \overline{\rm w}_{00}\boldsymbol{L}_{00} + \sum_{q,p}\overline{E}_{pq}(\overline{d}_{pq}\boldsymbol{M}_{pq} + \overline{c}_{pq}\boldsymbol{N}_{pq} + \overline{w}_{pq}\boldsymbol{L}_{pq}), \tag{9}$$

[1]There is a typo in Ref. [46], where the value of n_{st} should be $n_{st} = \max(|z|, n_c) + 15$.

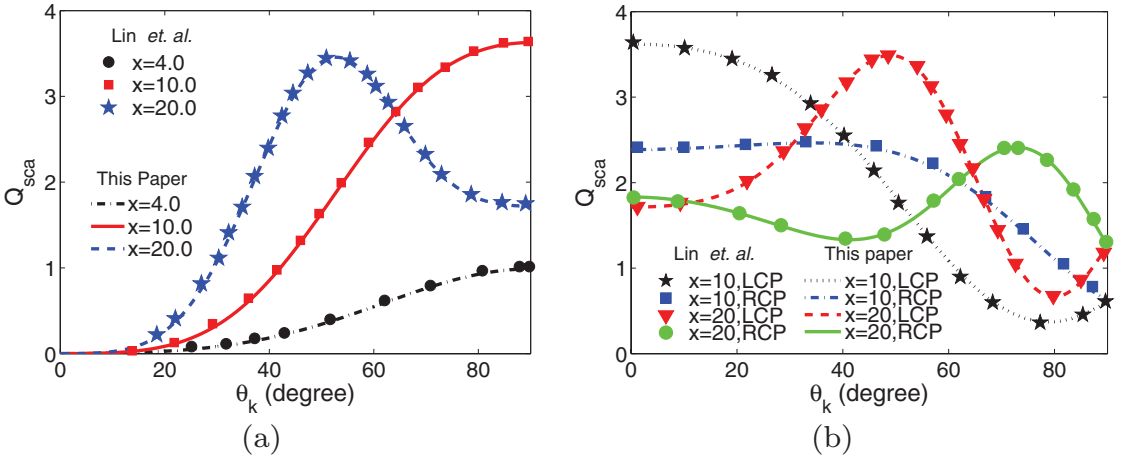

FIG. 3. (Color online) $Q_{\rm sca}$ versus θ_k at various values of x for (a) $\mu_g = 0$, $\mu_s\mu_t = \mu_0$, and $\mu_s = 1.4\mu_0$ with a polarization of $(p_\theta, p_\phi) = (0,1)$. (b) $\mu_g = 0.4$, $\mu_s = \mu_0$, and $\mu_t = 1$ with the same LCP and RCP polarizations as defined before.

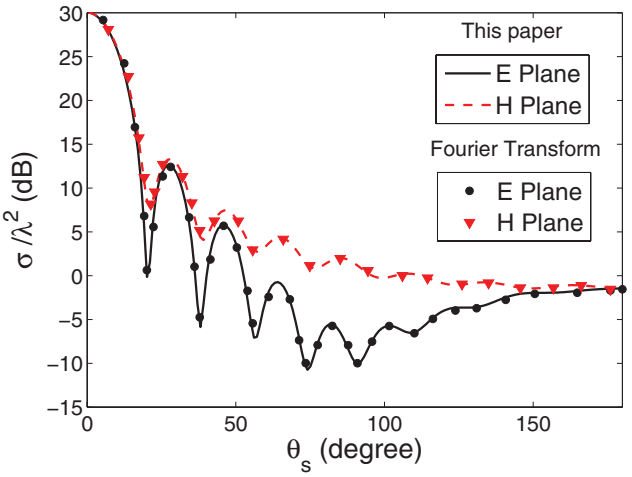

(a) A lossy gyroelectric sphere

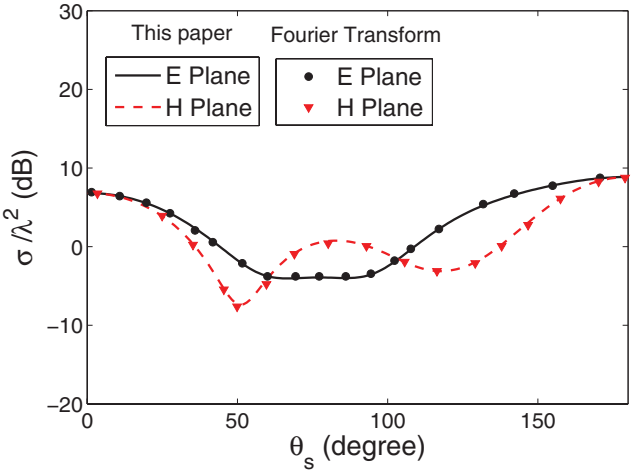

(b) A lossy LHM sphere

FIG. 4. (Color online) RCS versus scattering angle θ_s in the E and H planes with (a) $\mu_t = 1$, $\mu_g = 0$, $\mu_s = \mu_0$, $\epsilon_s = (1 + 0.5i)\epsilon_0$, $\epsilon_s\epsilon_t = (4 + 0.5i)\epsilon_0$, and $\epsilon_s\epsilon_g = 2\epsilon_0$ of $x = 3\pi$. (b) $\mu_t = 1$, $\mu_g = 0$, $\mu_s = -\mu_0$, $\epsilon_s = (-4 + 0.02i)\epsilon_0$, $\epsilon_s\epsilon_t = (-2 + 0.01i)\epsilon_0$, and $\epsilon_g = 0$ of electrical size parameter $x = 0.75\pi$.

where the expansion coefficients are expressed as follows:

$$\overline{d}_{pq} = \sum_{v,u} \frac{\overline{E}_{uv}}{\overline{E}_{pq}} \left(\tilde{g}^{uv}_{pq} d_{uv} + \overline{g}^{uv}_{pq} c_{uv} \right), \tag{10a}$$

$$\overline{c}_{pq} = \sum_{v,u} \frac{\overline{E}_{uv}}{\overline{E}_{pq}} \left(\tilde{e}^{uv}_{pq} d_{uv} + \overline{e}^{uv}_{pq} c_{uv} \right), \tag{10b}$$

$$\overline{w}_{pq} = \sum_{v,u} \frac{\overline{E}_{uv}}{\overline{E}_{pq}} \left(\tilde{f}^{uv}_{pq} d_{uv} + \overline{f}^{uv}_{pq} c_{uv} \right), \tag{10c}$$

$$\begin{aligned} \overline{\mathrm{w}}_{00} &= \sum_{v,u} \left[\overline{E}_{uv} \tilde{f}^{uv}_{00} d_{uv} + \overline{E}_{uv} \overline{f}^{uv}_{00} c_{uv} \right] \\ &= -\left[\left(\frac{2}{3} \right)^{\frac{1}{2}} \mu'_g d_{01} + \left(\frac{2}{15} \right)^{\frac{1}{2}} \overline{\mu'_t} c_{02} \right] E_0. \end{aligned} \tag{10d}$$

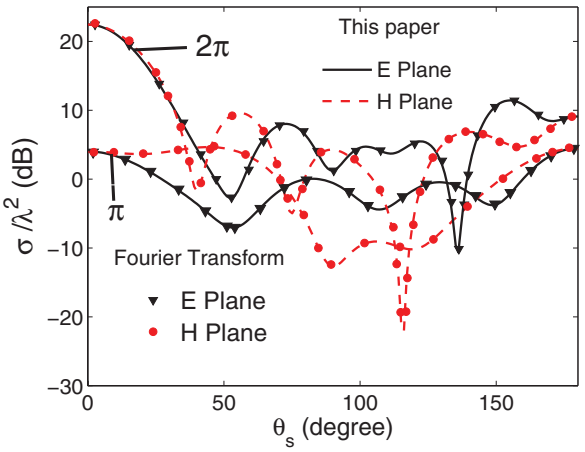

(a) A lossless uniaxial sphere

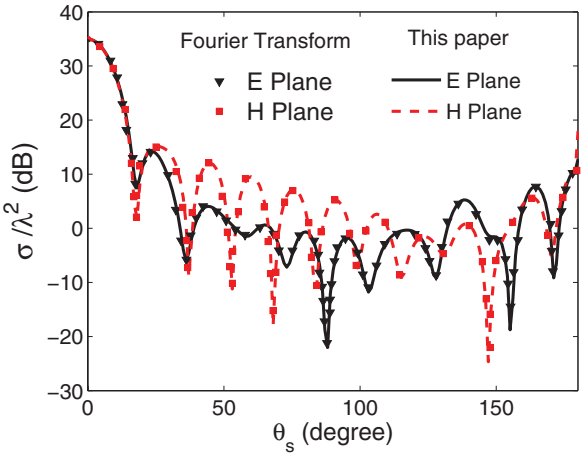

(b) An absorbing uniaxial sphere

FIG. 5. (Color online) RCS versus scattering angle θ_s in the E and H planes with $\mu_s = \mu_0$, $\mu_t = 1$, $\mu_g = 0$ and (a) the permittivity and permeability tensor elements are taken to be $\epsilon_s = 4.9284\epsilon_0$, $\epsilon_s\epsilon_t = 5.3495\epsilon_0$ and $\epsilon_g = 0$ and $(p_\theta, p_\phi) = (1,0)$. (b) $x = 4\pi$, $\epsilon_s = (4 + 0.2i)\epsilon_0$, $\epsilon_s\epsilon_t = (2 + 0.1i)\epsilon_0$ and $\epsilon_g = 0$ and $(p_\theta, p_\phi) = (1,0)$.

Since the spherical vector wave functions satisfy

$$\nabla \times \boldsymbol{M}^{(1)}_{mn} = k \boldsymbol{N}^{(1)}_{mn}, \tag{11a}$$

$$\nabla \times \boldsymbol{N}^{(1)}_{mn} = k \boldsymbol{M}^{(1)}_{mn}, \tag{11b}$$

$$\nabla \times \boldsymbol{L}^{(1)}_{mn} = 0, \tag{11c}$$

taking the curl of (9) and adopting the relations in (8a), we thus obtain[2]

$$\begin{aligned} &\epsilon_s \overline{\boldsymbol{\epsilon}}^{-1} \cdot (\nabla \times \mu_s \overline{\boldsymbol{\mu}}^{-1} \cdot \boldsymbol{B}_{\mathrm{int}}) \\ &\quad = k \sum_{n,m} \overline{E}_{mn} (\overline{\overline{c}}_{mn} \boldsymbol{M}_{mn} + \overline{\overline{d}}_{mn} \boldsymbol{N}_{mn} + \overline{\overline{w}}_{mn} \boldsymbol{L}_{mn}) + \overline{\overline{\mathrm{w}}}_{00} \boldsymbol{L}_{00}, \end{aligned} \tag{12}$$

[2]Note that there are some typos in the paper by Lin *et al.* [31]. The second column and row element of the inverse permeability tensor in (5) of their paper should read μ'_g instead of μ_g and the value of w_{00} should be multiplied by a factor of E_0.

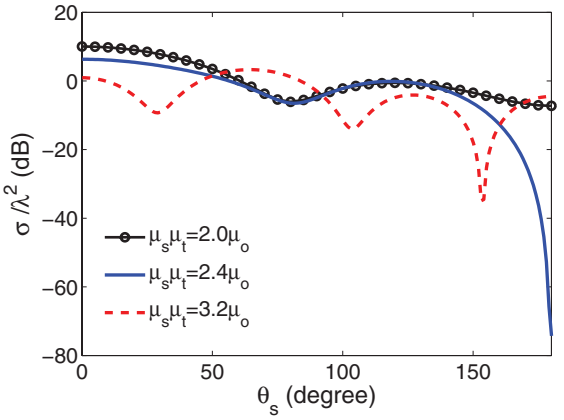

(a) Negative uniaxial sphere

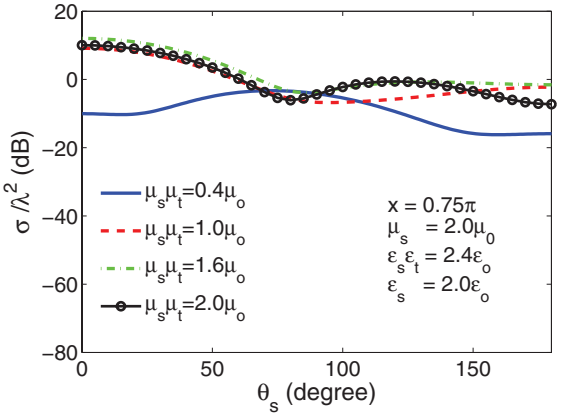

(b) Positive uniaxial sphere

FIG. 6. (Color online) RCS versus scattering angle with $A_e = 1.2$ for (a) magnetic negative uniaxial $A_m = 1.2$ (solid blue line), $A_m = 1.6$ (dashed red line), and nonmagnetic anisotropic case $A_m = 1.0$. (b) Magnetic positive uniaxial $A_m = 0.2$ (solid blue line), $A_m = 0.5$ (dashed red line), $A_m = 0.8$ (dashed-dotted green line) and nonmagnetic anisotropic case $A_m = 1$.

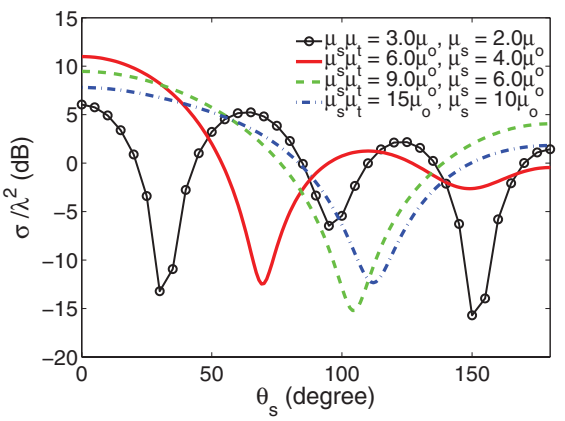

(a) Permeability multiplication factor effect

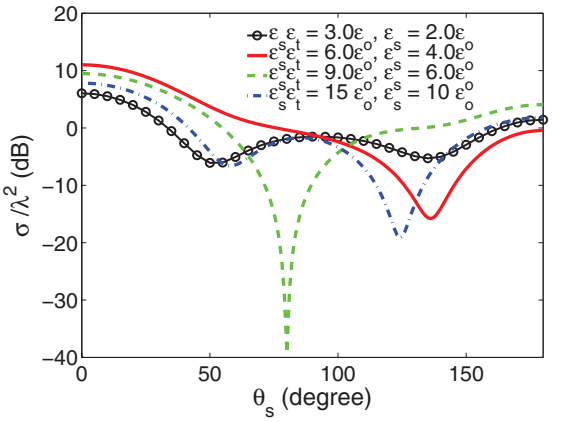

(b) Permittivity multiplication factor effect

FIG. 7. (Color online) The effect of (a) permeability multiplication factor with $\epsilon_s\epsilon_t = 2.4\epsilon_0$ and $\epsilon_s = 2.0\epsilon_0$ and (b) permittivity multiplication factor with $\mu_s\mu_t = 2.4\mu_0$ and $\mu_s = 2.0\mu_0$ on RCS. The multiplication factors are 1 (solid circle, black line), 2 (solid red line), 3 (dashed green line), and 5 (dashed-dotted blue line).

where

$$\bar{\bar{d}}_{mn} = \sum_{q,p} \frac{\overline{E}_{pq}}{\overline{E}_{mn}} \left(\overline{p}^{pq}_{mn}\overline{d}_{pq} + \tilde{p}^{pq}_{mn}\overline{c}_{pq}\right), \tag{13a}$$

$$\bar{\bar{c}}_{mn} = \sum_{q,p} \frac{\overline{E}_{pq}}{\overline{E}_{mn}} \left(\overline{o}^{pq}_{mn}\overline{d}_{pq} + \tilde{o}^{pq}_{mn}\overline{c}_{pq}\right), \tag{13b}$$

$$\bar{\bar{w}}_{mn} = \sum_{q,p} \frac{\overline{E}_{pq}}{\overline{E}_{mn}} \left(\overline{q}^{pq}_{mn}\overline{d}_{pq} + \tilde{q}^{pq}_{mn}\overline{c}_{pq}\right), \tag{13c}$$

$$\begin{aligned}\bar{\bar{w}}_{00} = -k\Bigg[&\sqrt{\frac{2}{15}}(\bar{\epsilon}_t' + \bar{\epsilon}_t'\bar{\mu}_t' + \epsilon_g'\mu_g')d_{02} \\ &+ \sqrt{\frac{2}{75}}\left(5\epsilon_g' + \epsilon_g'\bar{\mu}_t' + \bar{\epsilon}_t'\mu_g'\right)c_{01} \\ &+ \sqrt{\frac{16}{525}}(\epsilon_g'\bar{\mu}_t' + \bar{\epsilon}_t'\mu_g')c_{03}\Bigg]E_0.\end{aligned} \tag{13d}$$

By substituting (12) and (6) into (3) and making some simple manipulations, we obtain

$$\sum_{n,m} \overline{E}_{mn}\left[\tilde{\bar{d}}_{mn}\boldsymbol{M}^{(1)}_{mn}(k,\boldsymbol{r}) + \tilde{\bar{c}}_{mn}\boldsymbol{N}^{(1)}_{mn}(k,\boldsymbol{r})\right] = 0, \tag{14}$$

with

$$\begin{aligned}\tilde{\bar{d}}_{mn} = k^2 \sum_{q,p}\sum_{v,u} \frac{\overline{E}_{uv}}{\overline{E}_{mn}}\big[&\left(\overline{p}^{pq}_{mn}\tilde{g}^{uv}_{pq} + \tilde{p}^{pq}_{mn}\tilde{e}^{uv}_{pq}\right)d_{uv} \\ &+ \left(\overline{p}^{pq}_{mn}\overline{g}^{uv}_{pq} + \tilde{p}^{pq}_{mn}\overline{e}^{uv}_{pq}\right)c_{uv}\big] - k_s^2 d_{mn},\end{aligned} \tag{15a}$$

$$\begin{aligned}\tilde{\bar{c}}_{mn} = k^2 \sum_{q,p}\sum_{v,u} \frac{\overline{E}_{uv}}{\overline{E}_{mn}}\big[&\left(\overline{o}^{pq}_{mn}\tilde{g}^{uv}_{pq} + \tilde{o}^{pq}_{mn}\tilde{e}^{uv}_{pq}\right)d_{uv} \\ &+ \left(\overline{o}^{pq}_{mn}\overline{g}^{uv}_{pq} + \tilde{o}^{pq}_{mn}\overline{e}^{uv}_{pq}\right)c_{uv}\big] - k_s^2 c_{mn}.\end{aligned} \tag{15b}$$

In the matrix form, we have the following characteristic equation:

$$\begin{pmatrix}\tilde{\mathcal{P}} & \overline{\mathcal{P}} \\ \tilde{\mathcal{O}} & \overline{\mathcal{O}}\end{pmatrix}\begin{pmatrix}d \\ c\end{pmatrix} = \lambda\begin{pmatrix}d \\ c\end{pmatrix}, \tag{16}$$

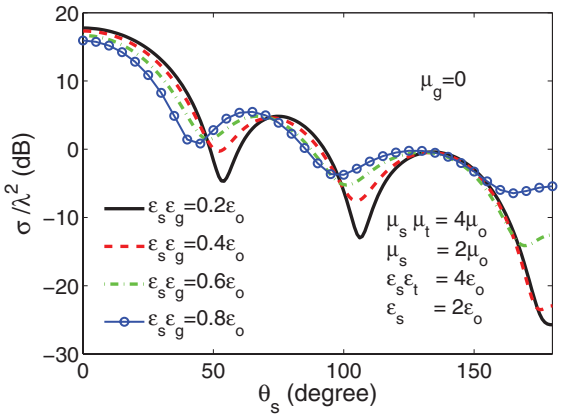

(a) Electric gyrotropy ratios

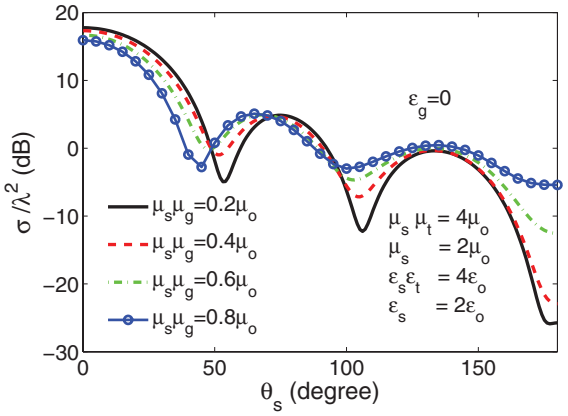

(b) Magnetic gyrotropy ratios

FIG. 8. (Color online) Effects of including gyrotropy ratios to a negative uniaxial sphere with $A_e = A_m = 2 > 1$ on RCS for (a) electric gyrotropy and (b) magnetic gyrotropy. The gyrotropy ratios are assumed to be 20 (solid black line), 10 (dashed red line), 6.67 (dashed-dotted green line), and 5 (circle blue line), respectively.

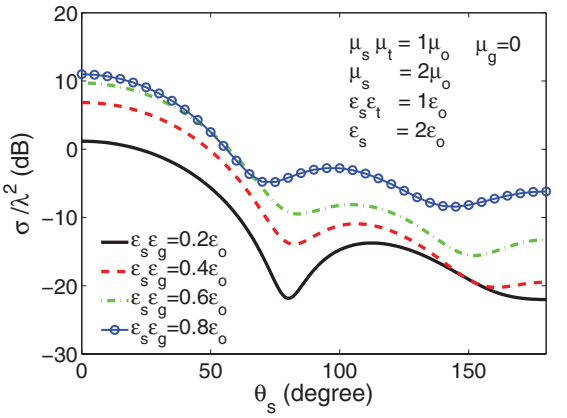

(a) Electric gyrotropy ratios

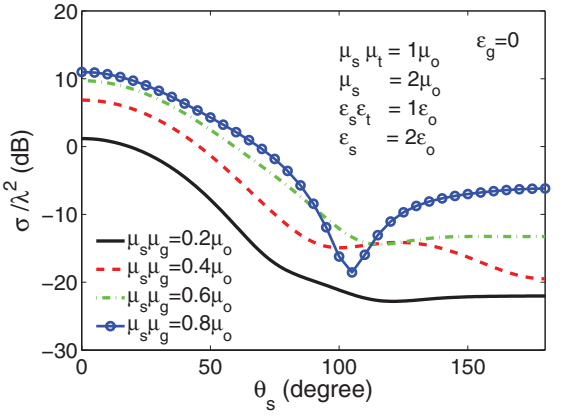

(b) Magnetic gyrotropy ratios

FIG. 9. (Color online) Effects of considering gyrotropy ratios to a positive uniaxial sphere with $A_e = A_m = 0.5$ on RCS for (a) electric gyrotropy and (b) magnetic gyrotropy. The gyrotropy ratios are 5 (solid black line), 2.5 (dashed red line), 1.67 (dashed-dotted green line), and 1.25 (circle blue line).

where $\lambda = k_s^2/k^2$, and the matrices $\tilde{\mathcal{O}}$, $\overline{\mathcal{O}}$, $\tilde{\mathcal{P}}$, and $\overline{\mathcal{P}}$ are defined by

$$\tilde{\mathcal{P}}_{mn,uv} = \sum_{q,p} \frac{\overline{E}_{uv}}{\overline{E}_{mn}} \left(\overline{p}^{pq}_{mn} \tilde{g}^{uv}_{pq} + \tilde{p}^{pq}_{mn} \tilde{e}^{uv}_{pq}\right), \tag{17a}$$

$$\overline{\mathcal{P}}_{mn,uv} = \sum_{q,p} \frac{\overline{E}_{uv}}{\overline{E}_{mn}} \left(\overline{p}^{pq}_{mn} \overline{g}^{uv}_{pq} + \tilde{p}^{pq}_{mn} \overline{e}^{uv}_{pq}\right), \tag{17b}$$

$$\tilde{\mathcal{O}}_{mn,uv} = \sum_{q,p} \frac{\overline{E}_{uv}}{\overline{E}_{mn}} \left(\overline{o}^{pq}_{mn} \tilde{g}^{uv}_{pq} + \tilde{o}^{pq}_{mn} \tilde{e}^{uv}_{pq}\right), \tag{17c}$$

$$\overline{\mathcal{O}}_{mn,uv} = \sum_{q,p} \frac{\overline{E}_{uv}}{\overline{E}_{mn}} \left(\overline{o}^{pq}_{mn} \overline{g}^{uv}_{pq} + \tilde{o}^{pq}_{mn} \overline{e}^{uv}_{pq}\right), \tag{17d}$$

with mn and uv denoting the row and column indices, respectively. Equation (16) is an eigensystem, with eigenvalues λ_l and eigenvectors $(d_{mn,l},\ c_{mn,l})^T$, where l denotes the index of eigenvalues and corresponding eigenvectors. We can then construct below a new eigenfunction $\boldsymbol{V}_l$ based on the eigenvectors:

$$\boldsymbol{V}_l = -\frac{k_l}{\omega} \sum_{n,m} \overline{E}_{mn} \left[d_{mn,l} \boldsymbol{M}^{(1)}_{mn}(k_l, \boldsymbol{r}) + c_{mn,l} \boldsymbol{N}^{(1)}_{mn}(k_l, \boldsymbol{r})\right], \tag{18}$$

where $k_l = k_s/\sqrt{\lambda_l}$. It is easy to show that $\boldsymbol{V}_l$ satisfies

$$\nabla \cdot \boldsymbol{V}_l = 0, \tag{19a}$$

$$\nabla \times [\epsilon_s \overline{\epsilon}^{-1} \cdot (\nabla \times \mu_s \overline{\mu}^{-1} \cdot \boldsymbol{V}_l)] - k_s^2 \boldsymbol{V}_l = 0. \tag{19b}$$

Thus, we can express the magnetic flux density $\boldsymbol{B}_{\rm int}$ inside the sphere as

$$\boldsymbol{B}_{\rm int} = \sum_{l=1}^{2n_d} \alpha_l \boldsymbol{V}_l, \tag{20}$$

where $n_d = n_c(n_c + 2)$ [48,49] and the expansion coefficients α_l are to be determined by matching the boundary conditions at the surface of the sphere. With the magnetic flux density $\boldsymbol{B}_{\rm int}$ given by (20), we can further write the magnetic field $\boldsymbol{H}_{\rm int}$[3] and the electric field $\boldsymbol{E}_{\rm int}$ both inside the

[3]In the $\mathbf{H}_l$ expression in [31], the last term should be *subtracted* instead of *added*.

sphere as

$$\boldsymbol{H}_{\rm int} = \overline{\boldsymbol{\mu}}^{-1}\cdot\boldsymbol{B}_{\rm int} = -\sum_{n,m}\overline{E}_{mn}\sum_{l}\alpha_l\frac{k_l}{\mu_s\omega}\big[\overline{d}_{mn,l}\boldsymbol{M}^{(1)}_{mn}(k_l,\boldsymbol{r}) + \overline{c}_{mn,l}\boldsymbol{N}^{(1)}_{mn}(k_l,\boldsymbol{r}) + \overline{w}_{mn,l}\boldsymbol{L}^{(1)}_{mn}(k_l,\boldsymbol{r})\big] - \sum_{l}\alpha_l\frac{k_l}{\mu_s\omega}\overline{\mathsf{w}}_{00,l}\boldsymbol{L}^{(1)}_{00}(k_l,\boldsymbol{r}), \tag{21a}$$

$$\boldsymbol{E}_{\rm int} = \frac{i}{\omega}\overline{\boldsymbol{\epsilon}}^{-1}\cdot(\nabla\times\boldsymbol{H}_{\rm int}) = -i\sum_{n,m}\overline{E}_{mn}\sum_{l}\alpha_l\frac{{k_l}^2}{\epsilon_s\mu_s\omega^2}\big[\overline{\overline{c}}_{mn,l}\boldsymbol{M}^{(1)}_{mn}(k_l,\boldsymbol{r}) + \overline{\overline{d}}_{mn,l}\boldsymbol{N}^{(1)}_{mn}(k_l,\boldsymbol{r}) + \overline{\overline{w}}_{mn,l}\boldsymbol{L}^{(1)}_{mn}(k_l,\boldsymbol{r})\big] - i\sum_{l}\alpha_l\frac{k_l^2}{\mu_s\epsilon_s\omega^2}\overline{\overline{\mathsf{w}}}_{00,l}\boldsymbol{L}^{(1)}_{00}(k_l,\boldsymbol{r}). \tag{21b}$$

In [31], the correct $\boldsymbol{H}_l$ expression should be expressed as follows:

$$\boldsymbol{H}_l = -\sum_{n=1}^{+\infty}\sum_{m=-n}^{+n}\frac{\alpha_l\epsilon_s\omega}{k_l}\sum_{l}\overline{E}_{mn}\Big[d_{mn,l}\boldsymbol{M}_{mn} + c_{mn,l}\boldsymbol{N}_{mn} + \frac{w_{mn,l}}{\lambda_l}\boldsymbol{L}_{mn}\Big] - \sum_{l}\alpha_l\frac{\omega\epsilon_s}{k_l}\frac{w_{00}}{\lambda_l}\boldsymbol{L}_{00}.$$

Note that due to the property in (11a) of spherical vector wave functions, we obtained another relation given by

$$\sum_{n,m}\overline{E}_{mn}\big[\tilde{\overline{d}}_{mn}\boldsymbol{N}^{(1)}_{mn}(k_l,\boldsymbol{r}) + \tilde{\overline{c}}_{mn}\boldsymbol{M}^{(1)}_{mn}(k_l,\boldsymbol{r})\big] = 0. \tag{22}$$

Therefore, (21b) can be further simplified to

$$\boldsymbol{E}_{\rm int} = -i\sum_{n,m}\overline{E}_{mn}\sum_{l}\alpha_l\Big[c_{mn,l}\boldsymbol{M}^{(1)}_{mn}(k_l,\boldsymbol{r}) + d_{mn,l}\boldsymbol{N}^{(1)}_{mn}(k_l,\boldsymbol{r}) + \frac{\overline{\overline{w}}_{mn,l}}{\lambda_l}\boldsymbol{L}^{(1)}_{mn}(k_l,\boldsymbol{r})\Big] - i\sum_{l}\alpha_l\Big[\frac{\overline{\overline{\mathsf{w}}}_{00,l}}{\lambda_l}\boldsymbol{L}^{(1)}_{00}(k_l,\boldsymbol{r})\Big]. \tag{23}$$

Since $\nabla\cdot\boldsymbol{H}_{\rm int}\neq 0$ and $\nabla\cdot\boldsymbol{E}_{\rm int}\neq 0$, their expansions include the term $\boldsymbol{L}_{mn}$, which is absent in the isotropic case.

B. Expansion of the scattered and incident fields

The scattered fields $\boldsymbol{E}_s$ and $\boldsymbol{H}_s$ and the incident fields $\boldsymbol{E}_i$ and $\boldsymbol{H}_i$ in the isotropic medium have the same form as those of the Mie theory [46,50]. The scattered fields are given explicitly as

$$\boldsymbol{E}_s = \sum_{n,m} i\overline{E}_{mn}\big[a_{mn}\boldsymbol{N}^{(3)}_{mn}(k_0,\boldsymbol{r}) + b_{mn}\boldsymbol{M}^{(3)}_{mn}(k_0,\boldsymbol{r})\big], \tag{24a}$$

$$\boldsymbol{H}_s = \frac{k_0}{\omega\mu_0}\sum_{n,m}\overline{E}_{mn}\big[b_{mn}\boldsymbol{N}^{(3)}_{mn}(k_0,\boldsymbol{r}) + a_{mn}\boldsymbol{M}^{(3)}_{mn}(k_0,\boldsymbol{r})\big], \tag{24b}$$

where $k_0^2 = \omega^2\epsilon_0\mu_0$. The coefficients a_{mn} and b_{mn} are to be determined by matching boundary conditions.

The incident fields considered in the paper are given by

$$\boldsymbol{E}_i = E_0(p_\theta\widehat{\boldsymbol{\theta}}_k + p_\phi\widehat{\boldsymbol{\phi}}_k)e^{i\boldsymbol{k}_0\cdot\boldsymbol{r}}, \tag{25a}$$

$$\boldsymbol{H}_i = \frac{k_0}{\omega\mu_0}E_0(p_\theta\widehat{\boldsymbol{\phi}}_k - p_\phi\widehat{\boldsymbol{\theta}}_k)e^{i\boldsymbol{k}_0\cdot\boldsymbol{r}}, \tag{25b}$$

where $\widehat{\boldsymbol{p}} = (p_\theta\widehat{\boldsymbol{\theta}}_k + p_\phi\widehat{\boldsymbol{\phi}}_k)$ denotes the normalized complex polarization vector with $|\widehat{\boldsymbol{p}}| = 1$, and the unit vectors $\widehat{\boldsymbol{\theta}}_k$ and $\widehat{\boldsymbol{\phi}}_k$ are defined in the direction of increasing θ_k and ϕ_k to constitute a right-hand-based system together with $\widehat{\boldsymbol{k}}_0 = \boldsymbol{k}_0/k_0$, as shown in Fig. 1. In terms of spherical vector wave functions, incident fields are expressed as

$$\boldsymbol{E}_i = -\sum_{n,m} i\overline{E}_{mn}\big[p_{mn}\boldsymbol{N}^{(1)}_{mn}(k_0,\boldsymbol{r}) + q_{mn}\boldsymbol{M}^{(1)}_{mn}(k_0,\boldsymbol{r})\big], \tag{26a}$$

$$\boldsymbol{H}_i = -\frac{k_0}{\omega\mu_0}\sum_{n,m}\overline{E}_{mn}\big[q_{mn}\boldsymbol{N}^{(1)}_{mn}(k_0,\boldsymbol{r}) + p_{mn}\boldsymbol{M}^{(1)}_{mn}(k_0,\boldsymbol{r})\big], \tag{26b}$$

where the coefficients p_{mn} and q_{mn} of incident wave and the details on their deduction can be found in [31], so they are omitted herewith.

C. Matching boundary conditions

The continuity of the tangential electric and magnetic field components at $r = a$ yields

$$p_{mn} = \Big[\frac{\xi_n'(x)}{\psi_n'(x)}\Big]a_{mn} + \sum_{l}\Big[\frac{1}{m_s\overline{k}_l}\frac{\psi_n'(\overline{k}_l m_s x)}{\psi_n'(x)}d_{mn,l}\Big]\alpha_l + \sum_{l}\Big[\frac{1}{m_s\overline{k}_l\lambda_l}\frac{j_n(\overline{k}_l m_s x)}{\psi_n'(x)}\overline{\overline{w}}_{mn,l}\Big]\alpha_l, \tag{27a}$$

$$q_{mn} = \Big[\frac{\xi_n(x)}{\psi_n(x)}\Big]b_{mn} + \sum_{l}\Big[\frac{1}{m_s\overline{k}_l}\frac{\psi_n(\overline{k}_l m_s x)}{\psi_n(x)}c_{mn,l}\Big]\alpha_l, \tag{27b}$$

$$p_{mn} = \Big[\frac{\xi_n(x)}{\psi_n(x)}\Big]a_{mn} + \sum_{l}\Big[\frac{\mu_0}{\mu_s}\frac{\psi_n(\overline{k}_l m_s x)}{\psi_n(x)}\overline{d}_{mn,l}\Big]\alpha_l, \tag{27c}$$

$$q_{mn} = \Big[\frac{\xi_n'(x)}{\psi_n'(x)}\Big]b_{mn} + \sum_{l}\Big[\frac{\mu_0}{\mu_s}\frac{\psi_n'(\overline{k}_l m_s x)}{\psi_n'(x)}\overline{c}_{mn,l}\Big]\alpha_l + \sum_{l}\Big[\frac{\mu_0}{\mu_s}\frac{j_n(\overline{k}_l m_s x)}{\psi_n'(x)}\overline{w}_{mn,l}\Big]\alpha_l, \tag{27d}$$

where the electrical size parameter is defined as $x = k_0 a$ and we also define

$$m_s = \frac{k_s}{k_0},\quad \overline{k}_l = \frac{k_l}{k_s},\quad m_s\overline{k}_l = \frac{k_l}{k_0},\quad \overline{k}_l m_s x = k_l a. \tag{28}$$

The Riccati-Bessel functions $\psi_n(z)$ and $\xi_n(z)$ were given by [46]

$$\psi_n(z) = z\,j_n(z)\quad\text{and}\quad \xi_n(z) = z h_n^{(1)}(z), \tag{29}$$

where $j_n(kr)$ and $h_n^{(1)}(kr)$ denote the spherical Bessel functions of the first and third kinds, respectively. Details on the numerical solutions of (27) can be found in [31].

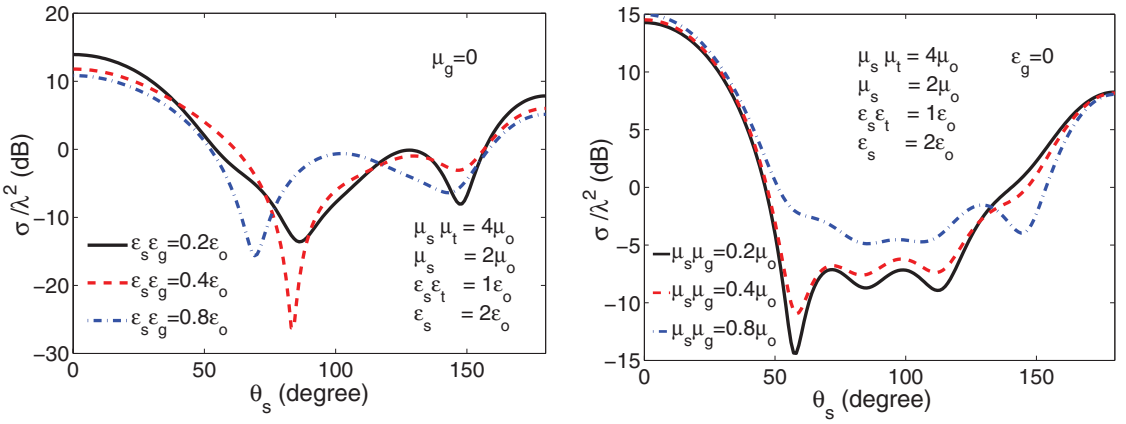

(a) Electric gyrotropy ratios (b) Magnetic gyrotropy ratios

FIG. 10. (Color online) Effects of adding gyrotropy ratios to a hybrid negative magnetic and positive electric uniaxial sphere of $A_e = 0.5 < 1$ and $A_m = 2.0 > 1$ on RCS. (a) Electric gyrotropy: $G_e = 5$ (solid black line), $G_e = 2.5$ (dashed red line), $G_e = 1.25$ (dashed-dotted blue line). (b) Magnetic gyrotropy: $G_m = 20$ (solid black line), $G_m = 10$ (dashed red line), and $G_m = 5$ (dashed-dotted blue line).

D. Scattering properties

From the coefficients of scattered fields, the scattering efficiency factor defined by

$$Q_{\text{sca}} = \frac{4}{x^2}\sum_{n,m}(|a_{mn}|^2 + |b_{mn}|^2), \tag{30}$$

and the radar cross sections (RCS's) defined [49] by

$$\sigma = \lim_{r\to\infty} 4\pi \frac{d\sigma_{\text{sca}}}{d\Omega}, \tag{31a}$$

$$\frac{d\sigma_{\text{sca}}}{d\Omega} = |\boldsymbol{f}(\theta,\phi)|^2, \tag{31b}$$

$$\boldsymbol{E}_s = E_0 \boldsymbol{f}(\theta,\phi)\frac{e^{ik_0 r}}{r}, \quad r\to\infty \tag{31c}$$

can be computed, where $(d\sigma_{\text{sca}})/(d\Omega)$ denotes the differential scattering cross section [31,51] and $\boldsymbol{f}(\theta,\phi)$ stands for the scattering amplitude. The asymptotic expressions of spherical vector wave functions, when $r \to \infty$, can be found from [52].

III. NUMERICAL RESULTS AND DISCUSSIONS

In the previous section, we have presented the necessary theoretical formulations of electromagnetic fields in the presence of a gyrotropic sphere. Validation is made and some typical results are presented in the paper to characterize effects of anisotropy ratios and gyrotropy ratios of lossless and lossy spherical scatterers.

An incident plane wave (of electric field amplitude equal to unity, polarized in parallel to the $+\hat{x}$ direction, and propagating in the $+\hat{z}$ direction) is assumed throughout the paper, and all the results presented herewith are those in the E plane (yoz) after verification section unless specified.

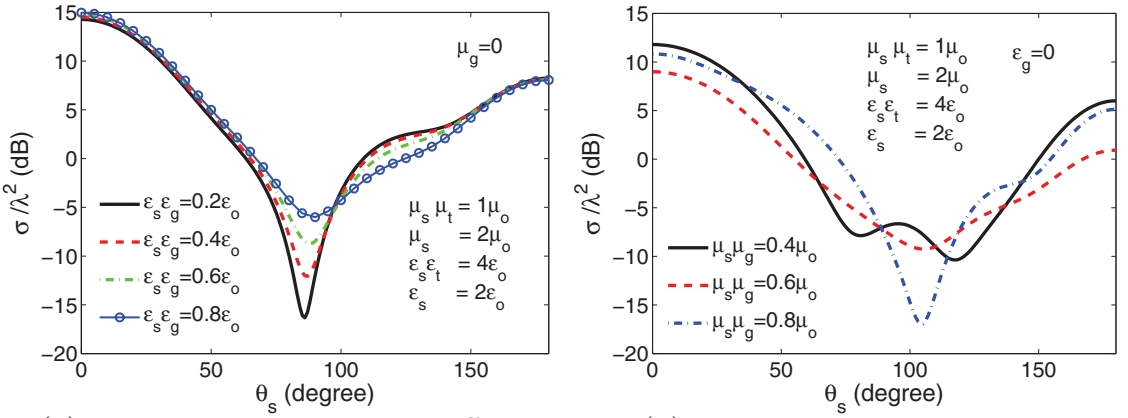

(a) Electric gyrotropy ratios effect (b) Magnetic gyrotropy ratios effect

FIG. 11. (Color online) Effects of taking into account gyrotropy ratios to a hybrid positive magnetic and negative electric uniaxial sphere of $A_e = 2.0 > 1$ and $A_m = 0.5 < 1$ on RCS for (a) electric gyrotropy: $G_e = 20$ (solid black line), $G_e = 10$ (dashed red line), $G_e = 6.67$ (dashed-dotted green line), $G_e = 5$ (solid circle blue line); and (b) magnetic gyrotropy: $G_m = 2.5$ (solid black line), $G_m = 1.67$ (dashed red line), and $G_m = 1.25$ (dashed-dotted blue line).

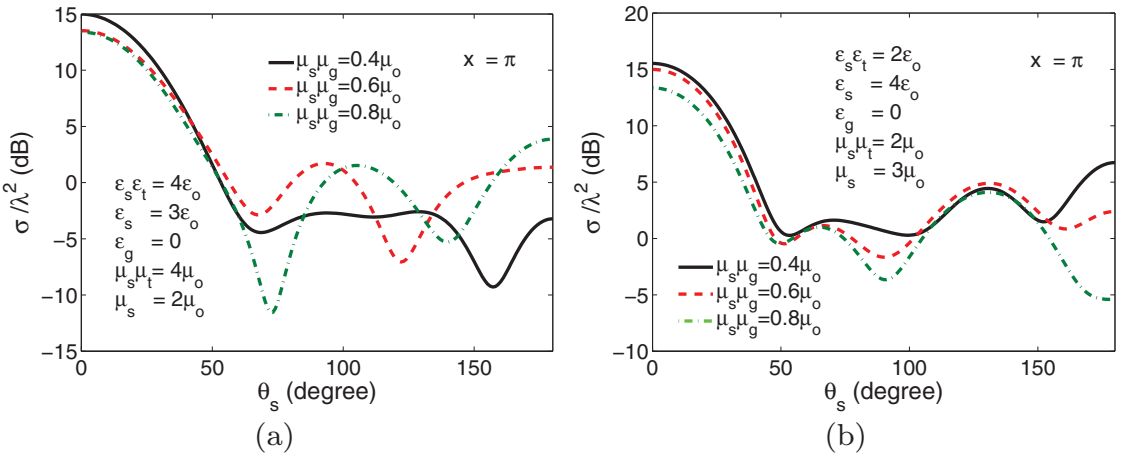

FIG. 12. (Color online) The dependency of RCS on gyrotropy ratios for (a) a hybrid negative sphere with $A_e = 1.33$ and $A_m = 2.0$ in the case of $G_m = 10$, $G_m = 6.67$, and $G_m = 5$, and (b) a hybrid positive sphere with $A_e = 0.5$ and $A_m = 0.67$ in the case of $G_e = 5$, $G_e = 3.33$, and $G_m = 2.5$.

A. Verifications

In order to validate our formulas and codes and also to check the accuracy of the obtained numerical results, we performed two trials. First, we reduce our solutions of gyrotropic sphere to gyromagnetic sphere with $\epsilon_s = \epsilon_0$, $\epsilon_t = 1$, and $\epsilon_g = 0$ as depicted in Figs. 2 and 3. Our results depict an exact match with the results obtained in Ref. [31].

Second, we compare our results with the published results of Geng *et al*. [27,53] and [28] for further validation purpose. They are depicted in Figs. 4 and 5, respectively. As can be clearly seen, an excellent agreement of the RCS values in the H plane (xoz) and the E plane (yoz) is achieved between our proposed solutions and the results obtained using the Fourier transform method adopted by Geng *et al*.

From these two trials, it partially verifies the correctness and applicability of our theory developed as well as our program codes written.

B. Lossless spherical scatterers

For a nonabsorbing or lossless spherical scatterer, all elements of $\overline{\epsilon}$ and $\overline{\mu}$ are real values. First, we investigate effects of joint anisotropy ratios (JARs) on radar cross section values, that is, $A_e = (\epsilon_s\epsilon_t)/\epsilon_s$ and $A_m = (\mu_s\mu_t)/\mu_s$. With this joint anisotropy ratio in place, we consider the single gyrotropy ratios (SGRs) $G_e = (\epsilon_s\epsilon_t)/(\epsilon_s\epsilon_g)$ or $G_m = (\mu_s\mu_t)/(\mu_s\mu_g)$, as well as joint gyrotropy ratios (JGRs), that is, G_e and G_m. Additionally, in order to understand better the role of JGR, we have considered a special case of JGR without anisotropy characteristic.

1. *Joint anisotropy effects*

In this section, the uniaxial cases are considered with size parameter $x = 0.75\pi$ and $\mu_g = \epsilon_g = 0$, $\epsilon_s\epsilon_t \neq \epsilon_s$, and $\mu_s\mu_t \neq \mu_s$. In Fig. 6, effects of joint anisotropy ratios are examined so as to demonstrate how the radar cross section is affected by the simultaneous presence of A_e and A_m. The radar cross section values due to a negative electric uniaxial with a negative magnetic uniaxial ($\mu_s\mu_t > \mu_s$) with a positive magnetic uniaxial ($\mu_s\mu_t < \mu_s$) are shown in Figs. 6(a) and 6(b), respectively. The values of $\overline{\epsilon}$ and μ_s are kept constant and $\mu_s\mu_r$ is changed so as to vary A_m, while A_e is fixed at 1.2. The single anisotropic case ($A_m = 1$ and $A_e = 1.2$) is included

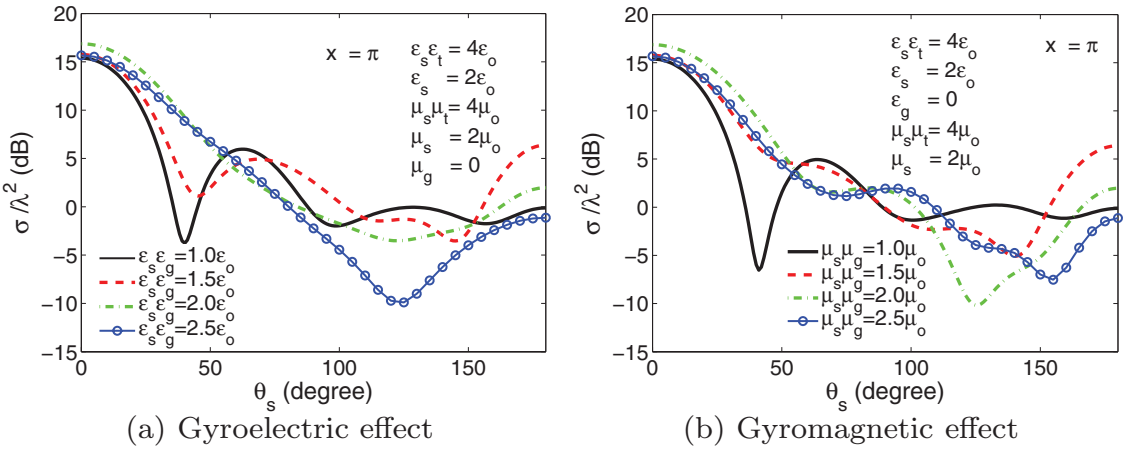

FIG. 13. (Color online) RCS versus scattering angle θ_s for a hybrid negative uniaxial sphere $A_m = A_e = 2$ for gyrotropic cross term greater than 1. (a) $G_e = 4.0$, $G_e = 2.67$, $G_e = 2.0$, and $G_e = 1.6$; (b) $G_m = 4.0$, $G_m = 2.67$, $G_m = 2.0$, and $G_m = 1.6$.

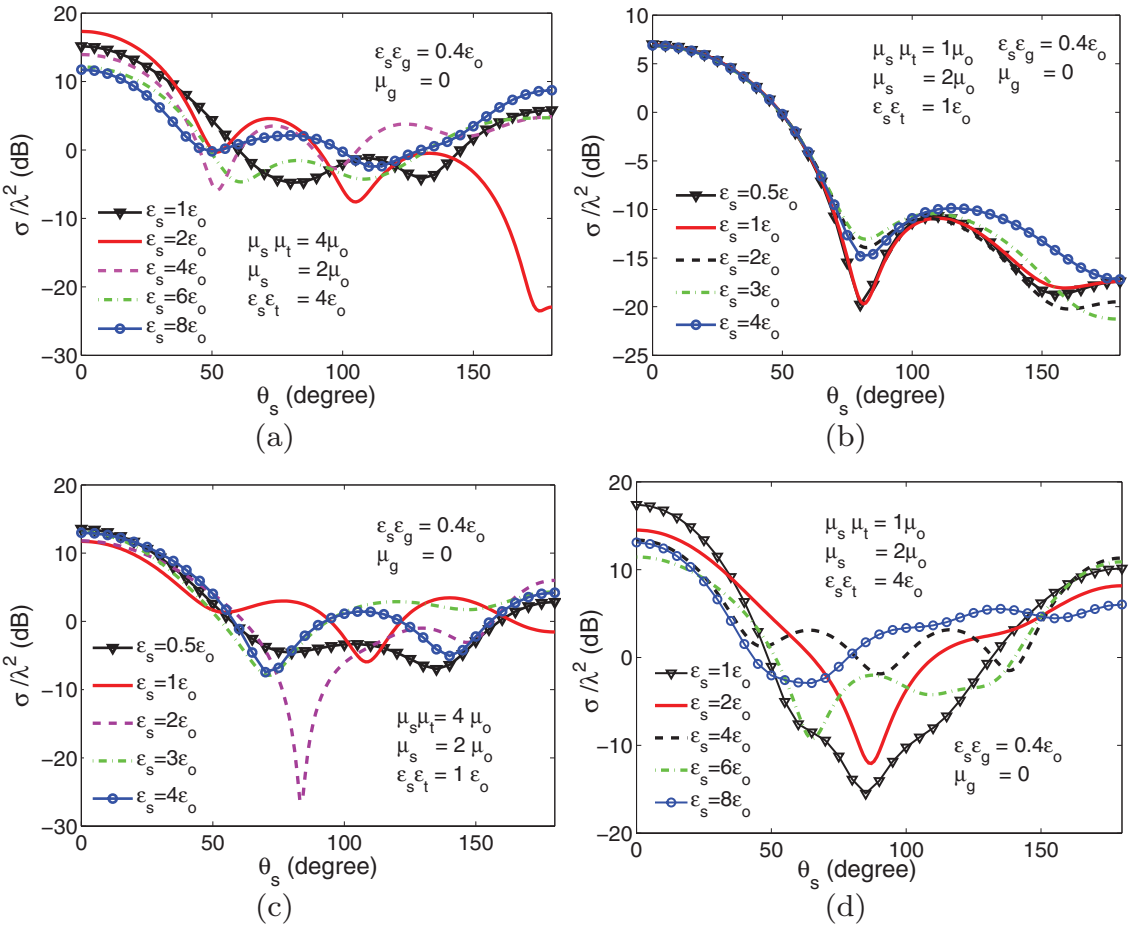

FIG. 14. (Color online) Effects of electric anisotropy ratios of a hybrid gyroelectric and uniaxial magnetic sphere on RCS for (a) $A_m = 2$ and $G_e = 10$, (b) $A_m = 0.5$ and $G_e = 2.5$, (c) $A_m = 2$ and $G_e = 2.5$, (d) $A_m = 0.5$ and $G_e = 10$. The electric anisotropy ratios for Figs. 14(a) and 14(d) are $A_e = 4$, 2, 1, 0.67, and 0.5 whereas for Fig. 14(b) and 14(c) are $A_e = 2$, 1, 0.5, 0.33, and 0.25.

for comparison purposes. Observe that there is a great resonance reduction (decreases of 80 dB compared to the single electric uniaxial $A_m = 1$ and $A_e = 1.2$) in the backscattering for $A_m = 1.2$ that will be useful in military applications. By comparing positive ($A_m < 1$) and negative ($A_m > 1$) magnetic uniaxials, sharper oscillations can be seen for $A_m > 1$.

Figure 7 depicts effects of multiplication factors of $\overline{\overline{\mu}}$ on radar cross section with $\epsilon_s\epsilon_t = 2.4\epsilon_0$ and $\epsilon_s = 2.0\epsilon_0$ in Fig. 7(a) and of $\overline{\overline{\epsilon}}$ with $\mu_s\mu_t = 2.4\mu_0$ and $\mu_s = 2.0\mu_0$ in Fig. 7(b). It is observed that the resonances shift to the right when the multiplication factor for $\overline{\overline{\mu}}$ increases from 1 to 5. However, these properties do not apply for $\overline{\overline{\epsilon}}$ in Fig. 7(b).

2. *Single gyrotropy effects*

In this section, the electrical size parameter of $x = \pi$ is assumed and gyrotropic cross-coupling terms are included to either $\overline{\overline{\mu}}$ or $\overline{\overline{\epsilon}}$. Figure 8 shows the dependence of the RCS on gyrotropy ratios. It is found that the reduction in G_e or G_m of the same joint negative anisotropy ratios $A_e = A_m = 2 > 1$ leads to enhancement of the RCS level particularly at the scattering angles of $\theta_s \approx 110^\circ$ and 180°.

As compared to Fig. 8, there is less oscillation for a positive uniaxial sphere as portrayed in Fig. 9. Also, opposite behavior in Fig. 9 is shown in the forward scattering, as compared with that in Fig. 8 (where RCS level increases as gyrotropy ratios decrease at $\theta_s = 0^\circ$); but the same characteristics in the backward scattering in Figs. 8 and 9 are observed (where RCS level increases as gyrotropy ratios decreases at $\theta_s = 180^\circ$).

Interestingly, when we consider an opposite combination type of anisotropy (that is, hybrid of positive electric uniaxial and negative magnetic uniaxial sphere) as displayed in Fig. 10, there is an increment in RCS level from $\theta_s \approx 55^\circ$ to 130° as G_m decreases as described in Fig. 10(b). This may be due to negative magnetic anisotropy ratios or higher magnetic gyrotropy ratios in the gyromagnetic case as compared to the gyroelectric case. Also, it is observed that the forward and backward RCS are less sensitive to magnetic gyrotropy ratios as there is little variation at scattering angles $\theta_s = 0^\circ$ and 180°. However, such observations do not exist as we decrease G_e in Fig. 10(a). On the contrary, $G_e = 2.5$ reduces the RCS level of $G_e = 5$ in the vicinity of $\theta_s \approx 90^\circ$.

Figure 11 has almost similar trends as Fig. 10, in which the increment of RCS level at resonances when gyrotropy ratios decrease only happens for the case of positive anisotropy and higher gyrotropy ratios in Fig. 11(a). On the other hand, the RCS level at $\theta_s \approx 100^\circ$ is being suppressed as G_m decreases from 2.5 to 1.25. In fact, an irregular variation of RCS values can be seen for the case of varying gyrotropy ratios as illustrated in Fig. 11(b).

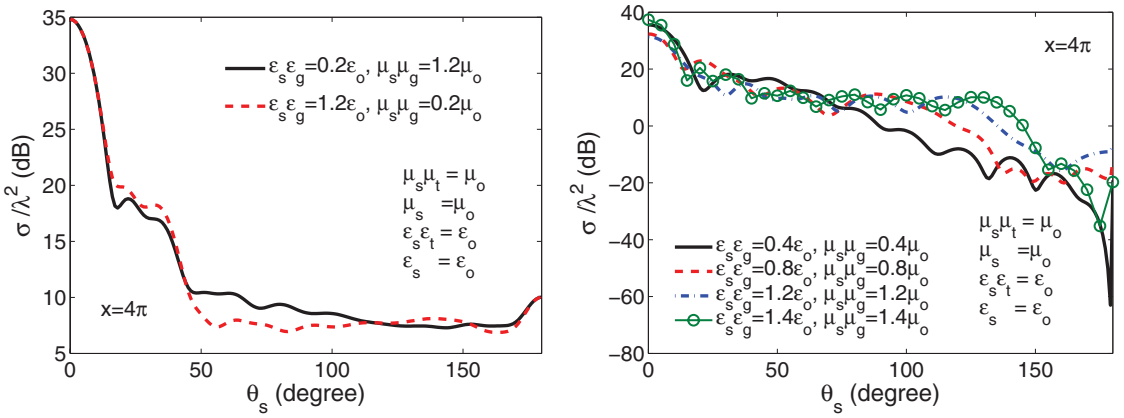

(a) Different magnetic and electric gyrotropy ratios

(b) Same magnetic and electric gyrotropy ratios

FIG. 15. (Color online) Effects of gyrotropy ratios on RCS values without anisotropy effect, $A_e = A_m = 1$, of size parameter $x = 4\pi$: (a) $G_e = 5 > G_m = 0.83$ (solid black line) and $G_e = 0.83 < G_m = 5$ (dashed red line). (b) $G_e = G_m$ of the following values: 2.5 (solid black line), 1.25 (dashed red line), 0.833 (dashed-dotted blue line), and 0.714 (solid circle green line).

In Fig. 12, we reveal effects of gyrotropy ratios in the case that $A_e \neq A_m$, but both belong to a negative lossless anisotropic sphere in Fig. 12(a) and a positive lossless anisotropic sphere in Fig. 12(b). It is noted that effects of magnetic gyrotropy ratios on RCS values are of an irregular form and unpredictable for the negative anisotropic sphere. For the positive anisotropic sphere, there is a slight suppression of forward scattering, and effects of suppression are getting larger for the backward scattering when G_m decreases.

Figure 13 showcases the functions of the gyrotropic cross term when their values are greater than 1. Generally, there is no regular behavior being spotted. However, it can be seen that the RCS values are quite sensitive to the changes in gyrotropy ratios.

Different combinations of electric gyrotropy and magnetic anisotropy ratios are considered and their effects are depicted in Fig. 14. It appears that RCS values are quite sensitive to the electric anisotropy A_e except when $A_m = 0.5$ and $G_e = 2.5$ in Fig. 14(b) and the scattering characteristics of a lossless sphere are significantly affected by the presence of anisotropy.

3. *Hybrid gyrotropy effects*

First, we consider RCS results solely due to gyrotropy effects whereby the anisotropy ratios are set to be $A_e = A_m = 1$ for a very large-sized sphere, where $x = 4\pi$. The results are shown in Fig. 15. Figure 15(a) shows a drastic drop (by 25 dB) in RCS level at the beginning, which almost flattens in the middle at around RCS level of 5 dB and begins to increase only slightly at the end. Notice that the case of $G_e = 0.83 < G_m = 5$ undergoes more damping as it becomes nearly flat much faster than the case where $G_e = 5 > G_m = 0.83$. If the same gyrotropy ratios are considered simultaneously, i.e., $G_e = G_m$, the backscattering increases as the gyrotropy ratio decreases.

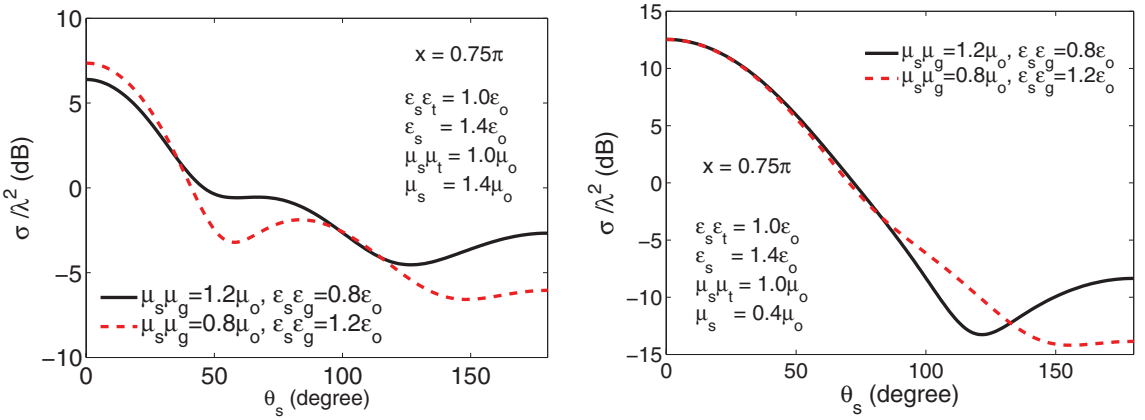

(a) Positive anisotropic sphere

(b) Positive electric and negative magnetic anistropic sphere

FIG. 16. (Color online) Effects of different magnetic and electric gyrotropy and anisotropy ratios on RCS values: (a) $A_e = A_m = 0.714 < 1$ for $G_e = 1.25 > G_m = 0.83$ (solid black line) and $G_e = 0.83 < G_m = 1.25$ (dashed red line). (b) $A_e = 0.714 < 1$ and $A_m = 2.5 > 1$ for $G_e = 1.25 > G_m = 0.83$ (solid black line) and $G_e = 0.83 < G_m = 1.25$ (dashed red line).

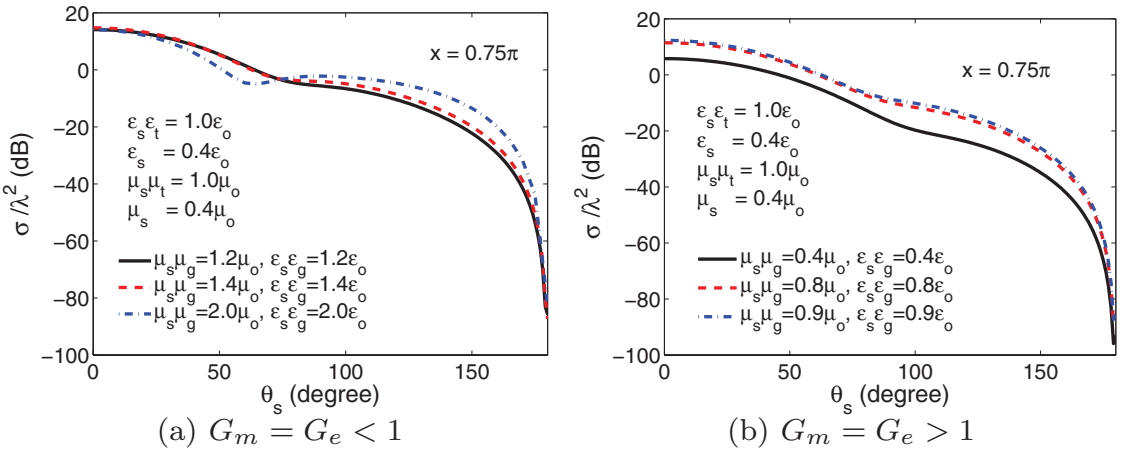

(a) $G_m = G_e < 1$ (b) $G_m = G_e > 1$

FIG. 17. (Color online) Effects of the same magnetic and electric gyrotropy ratios ($A_m = A_e = 2.5$) for a negative anisotropy sphere on RCS values: (a) $G_m = G_e < 1$ for 0.83 (solid black line), 0.714 (dashed red line), and 0.50 (dashed-dotted blue line). (b) $G_m = G_e > 1$ for 2.4 (solid black line), 1.25 (dashed red line), and 1.11 (dashed-dotted blue line).

There is little variation for the first half of the scattering angles from $\theta_s = 0^\circ$ to 90°.

Next, we include JAR effects into the JGR for some special cases. The results for different gyrotropy ratios and anisotropy ratios are illustrated in Fig. 16. As compared to the previous nonanisotropy case in Fig. 15(a), the drop is not so drastic at the beginning. This may be due to a large difference between electric and magnetic gyrotropy ratios or to nonexistence of anisotropy effect for Fig. 15(a). Additionally, the case of $G_e = 0.83 < G_m = 1.25$ is much damper than the case of $G_e = 1.25 > G_m = 0.83$. These properties are similar to those of the nonanisotropy case.

Hybrid magnetic and electric gyrotropy ratios of the same value are considered in Fig. 17. It is discovered that when gyrotropy ratios decrease as displayed in Fig. 17(b), there is an enhancement in RCS level. Nevertheless, at the beginning of the $G_m = G_e < 1$ case depicted in Fig. 17(a), this does not hold and it seems that there is a tendency to decrease the RCS further if we further decrease the gyrotropy ratios.

C. Lossy spherical scatterers

For an absorbing or lossy spherical scatterer, the elements in $\overline{\epsilon}$ and $\overline{\mu}$ are complex in value. The imaginary parts represent absorptions. Subsequently, we will first study characteristics of JAR followed by SGR and JGR, respectively. On top of that, we also present the scattering efficiencies $Q_{\rm sca}(\theta_k)$ at an incident angle of $\theta_k = 0^\circ$ versus size parameter x for lossless and lossy spheres.

1. Joint anisotropy effects

Figure 18 shows the effect of joint anisotropy effect on RCS. In Fig. 18(a), the value of A_e is kept constant and A_m changed so as to see the effect of A_m on RCS. It is shown that when A_m decreases, the backscattering increases. This is the same for the effect of changing A_e and keeping A_m constant.

2. Single gyrotropy effects

Herein, we consider only the gyrotropic cross term in either $\overline{\mu}$ or $\overline{\epsilon}$ and the other parameters remain as those of uniaxial

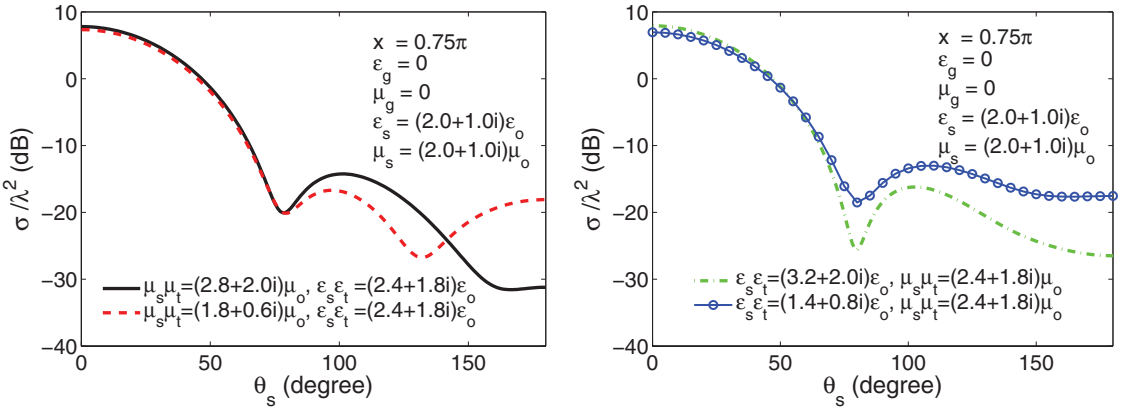

(a) A_m effect (b) A_e effect

FIG. 18. (Color online) Effects of joint anisotropy ratios on RCS values for an absorbing uniaxial sphere. (a) Solid black line: $A_e = 1.32 + 0.24i$ and $A_m = 1.52 + 0.24i$; dashed red line: $A_e = 1.32 + 0.24i$ and $A_m = 0.84 - 0.12i$. (b) Dashed-dotted green line: $A_e = 1.68 + 0.16i$ and $A_m = 1.32 + 0.24i$; solid circle blue line: $A_e = 0.72 + 0.04i$ and $A_m = 1.32 + 0.24i$.

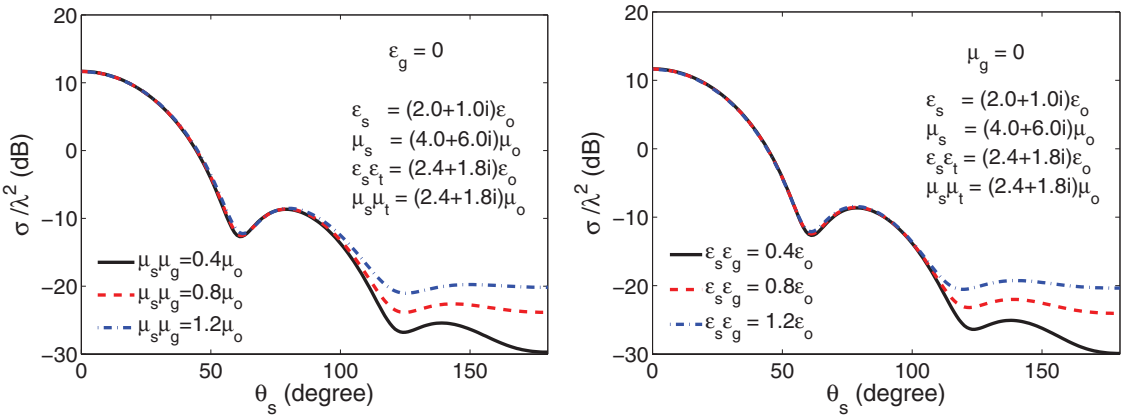

(a) Gyromagnetic effect (b) Gyroelectric effect

FIG. 19. (Color online) Effects of gyrotropy ratios for a hybrid anisotropic sphere ($A_e = 1.32 + 0.24i$ and $A_m = 0.392 - 0.138i$) on RCS values. (a) Solid black line: $G_m = 6.0 + 4.5i$; dashed red line: $G_m = 3.0 + 2.25i$; dashed-dotted blue line: $G_m = 2.0 + 1.5i$. (b) Solid black line: $G_e = 6.0 + 4.5i$; dashed red line: $G_e = 3.0 + 2.25i$; dashed-dotted blue line: $G_e = 2.0 + 1.5i$.

ones. In Fig. 19, it is observed that the RCS level approaches a more or less stable value after $\theta_s \approx 130^\circ$. The higher the gyrotropy ratios G_m in Fig. 19(a) or G_e in Fig. 19(b), the lower the backscattering level.

3. *Joint gyrotropy effects*

Instead of a single gyrotropy, we add gyrotropic cross terms to both $\overline{\boldsymbol{\mu}}$ and $\overline{\boldsymbol{\epsilon}}$. Similar properties to Fig. 19 are obtained, as shown in Fig. 20.

Figure 21 shows the results of RCS values for a negative magnetic lossy sphere ($\mu_s\mu_t > \mu_s$) and a positive magnetic lossy sphere ($\mu_s\mu_t < \mu_s$) with increasing imaginary part (or loss tangent) of the complex permittivity $\mu_s\mu_t$. In Fig. 21(a), the negative magnetic lossy sphere exhibits lower oscillations as compared to the positive magnetic lossy sphere in Fig. 21(b). Moreover, as the imaginary part of the complex permittivity $\mu_s\mu_t$ for the negative magnetic lossy sphere increases, the RCS level gradually increases with scattering angle and eventually approaches their own constant values of -10.40, -8.966, and -7.791 dB, respectively. However, for the positive absorbing sphere, this characteristic only occurs in the first half region of the scattering angles and then gradually decreases during the second half region and converges to a single RCS value, i.e., -7.49 dB.

Figure 22 presents the values of $Q_{\text{sca}}(0^\circ)$ for different size parameters x of a gyrotropic lossless and lossy sphere. It is observed that the lossless gyrotropic sphere shows an irregular fluctuation and the oscillations do not end up with a stable value. On the other hand, the lossy case reaches a stable value approximately 1 when x increases.

D. Summary

From all these observations as above, it can be concluded that scattering characteristics of lossless and lossy spheres are certainly affected by the presence of anisotropy and gyrotropy ratios of these spheres. By studying many different cases for a

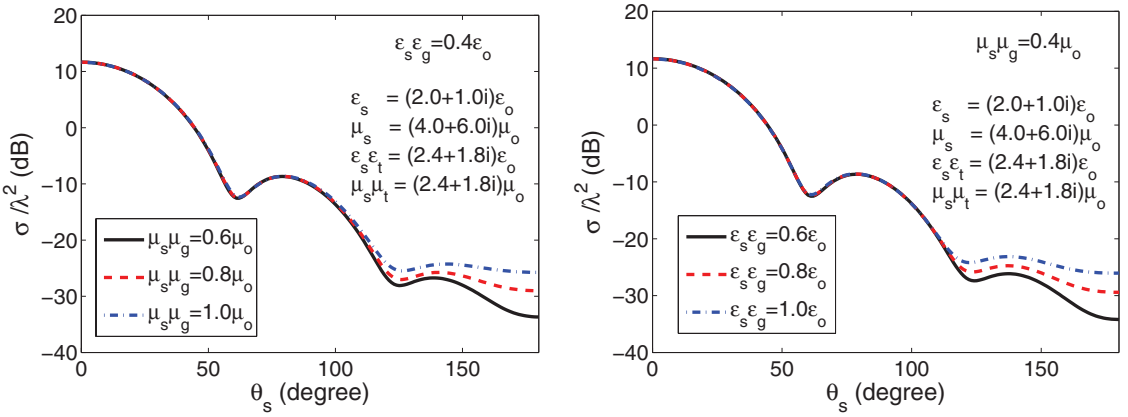

(a) (b)

FIG. 20. (Color online) Effects of joint gyrotropy ratios for a hybrid anisotropic sphere ($A_e = 1.32 + 0.24i$ and $A_m = 0.392 - 0.138i$) on RCS values. (a) $G_e = 6.0 + 4.5i$ and $G_m = 4.0 + 3.0i$ (solid black line); $G_m = 3.0 + 2.25i$ (dashed red line); $G_m = 2.4 + 1.8i$ (dashed-dotted blue line). (b) $G_m = 6.0 + 4.5i$ and $G_e = 4.0 + 3.0i$ (solid black line); $G_e = 3.0 + 2.25i$ (dashed red line); $G_e = 2.4 + 1.8i$ (dashed-dotted blue line).

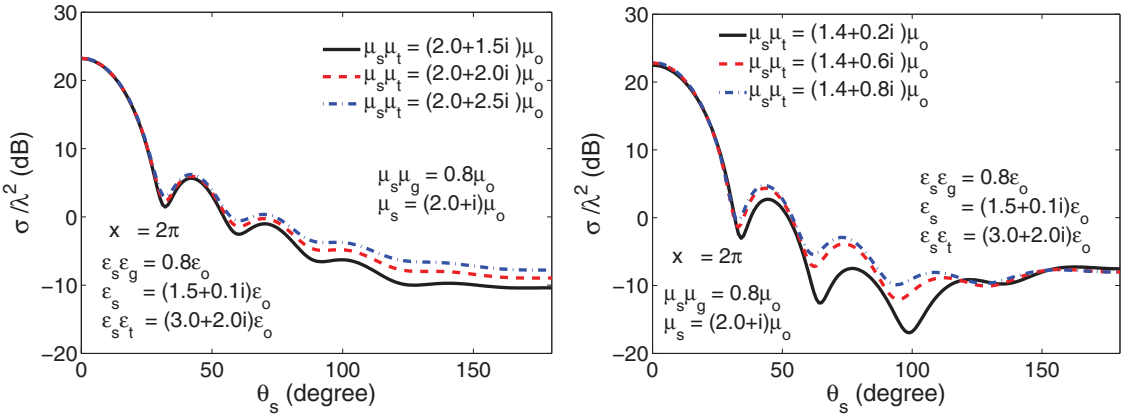

(a) Negative magnetic lossy sphere (b) Positive magnetic lossy sphere

FIG. 21. (Color online) RCS values versus scattering angle θ_s for a hybrid gyrotropic and anisotropic absorbing sphere when the imaginary part of $\mu_s\mu_t$ is increased. (a) A negative magnetic lossy sphere. (b) A positive magnetic lossy sphere.

wide range of anisotropy and gyrotropy effects, it is apparent that the dependence of radar cross sections on anisotropy and gyrotropy is very complicated in form, and what we observed is resulted in by hybrid parametric effects. For practical scientific and engineering applications, scattering characteristics are predictable and controllable by varying physical and electric parameters of the scattering system and sometimes optimizations are necessary to achieve maximum or minimum RCS value(s).

From some of the special cases considered here, certain physical characteristics of the gyrotropic sphere can be summarized.

(i) First, oscillations are much sharper for JAR of the negative magnetic uniaxial and negative electric uniaxial spheres as shown in Fig. 6 for the uniaxial case and Figs. 8 and 9 for the single gyrotropy cases.

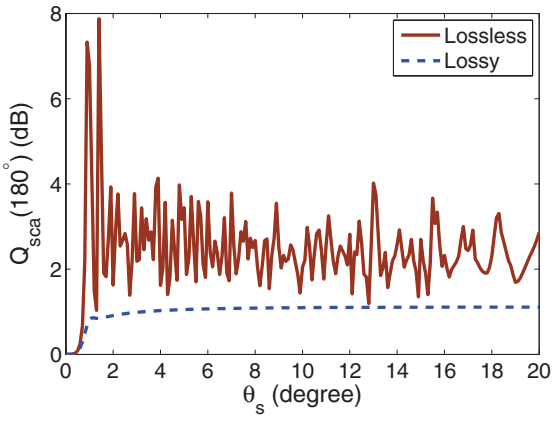

FIG. 22. (Color online) Scattering efficiencies $Q_{\rm sca}(0^\circ)$ versus the size parameter x for lossless and lossy spheres. The permeability and permittivity elements are assumed to be $\epsilon_s\epsilon_t = 3\epsilon_0$, $\epsilon_s = 5\epsilon_0$, $\mu_s\mu_t = 3\mu_0$, $\mu_s = 5\mu_0$, $\epsilon_s\epsilon_g = 0.8\epsilon_0$, and $\mu_s\mu_g = 0.8\mu_0$ for a lossless sphere; and $\epsilon_s\epsilon_t = (2.4 + 1.08i)\epsilon_0$, $\epsilon_s = (4.0 + 1.8i)\epsilon_0$, $\epsilon_s\epsilon_g = 0.8\epsilon_0$, $\mu_s\mu_t = (2.4 + 1.08i)\mu_0$, $\mu_s = (4.0 + 1.8i)\mu_0$, and $\mu_s\mu_g = 0.8\mu_0$ for a lossy sphere.

(ii) Second, for SGR of a lossless sphere, RCS increases in the vicinity of the resonance as gyrotropy ratios decrease when $(A_e = A_m) > 1$, which is shown in Fig. 8. Also, if different types of JAR are considered, the magnetic or electric positive anisotropy with higher gyrotropy ratios will cause this behavior. For instance, RCS intensifies around the resonances when G_e decreases for the hybrid anisotropic sphere of $A_e > 1$ and $A_m < 1$, as shown in Fig. 11.

(iii) In addition, when the gyrotropy ratio for a lossy sphere decreases, the RCS level gradually increases at and after scattering angle of 90° and eventually approaches its own constant values for (a) the single gyrotropy case, as depicted in Fig. 19 and (b) the joint gyrotropy case, as illustrated in Fig. 20.

(iv) Lastly, for JGR, $G_e < G_m$ will undergo more damping than $G_e > G_m$ for the nonanisotropy case shown in Fig. 15 and with the incorporation of JAR displayed in Fig. 20.

IV. CONCLUSIONS

In conclusion, solutions for characterizing anisotropic effects of Lorentz-Mie scattering of electromagnetic plane waves by a gyrotropic sphere are derived theoretically by employing the multiple scattering spheres method together with the T-matrix method. It should be pointed out that with both permittivity and permeability tensors considered, the problem defined herewith is very generalized physically, quite difficult mathematically, and much complicated and involved numerically, as compared with those available in literature [31–33,35]. Validations of the generalized solutions are conducted, where numerical results are then yielded from the formulas and found to agree very well with those of the Fourier transform method during result validations. New examples are also considered and their physical insights are obtained and analyzed. The present numerical results have uncovered various physical effects of joint anisotropy ratio (JAR), single gyrotropy ratio (SGR), and joint gyrotropy ratio (JGR) and provided deeper physical insights into utilizing these physical and electrical parameters and controlling scattering properties

so as to *minimize* or *enhance* radar cross sections in practical applications. Of course, there are too many physical and electric factors affecting hybrid RCS characteristics of the sphere, therefore, different combinations of these factors will lead to various different physical insights. This paper focuses on the theoretical aspects of the problem solution, while the numerical solutions provide validations of theoretical results and also partial new physical insights. The present parametric studies serve as an initial exploration of new physics, but further understanding of comprehensive information about scattering characterizations will be expected in the future.

ACKNOWLEDGMENTS

The authors are also grateful to the useful discussions with Dr. C. Wan at the National University of Singapore. J. L. W. Li is also grateful to financial support in terms of a Qian-Ren-Ji-Hua Chair Professorship or National Professorship by Chinese Government's 1000-Talent Plan via the University of Electronic Science and Technology of China, Chengdu 611731, China.

APPENDIX

With $\bar{\epsilon}_t' = \epsilon_t' - 1$, some intermediate coefficients are obtained and expressed as follows:

$$\tilde{o}_{pq}^{mn} = \delta_{nq}\delta_{mp} + \left[\frac{(n^2+n-m^2)\bar{\epsilon}_t' + m\epsilon_g'}{n(n+1)}\right]\delta_{nq}\delta_{mp}, \quad \text{(A1a)}$$

$$\tilde{p}_{pq}^{mn} = \frac{i(n+m)[m\bar{\epsilon}_t' - (n+1)\epsilon_g']\delta_{n-1,q}\delta_{mp}}{n(2n+1)} + \frac{i(n-m+1)[m\bar{\epsilon}_t' + n\epsilon_g']\delta_{n+1,q}\delta_{mp}}{(n+1)(2n+1)}, \quad \text{(A1b)}$$

$$\tilde{q}_{pq}^{mn} = \frac{-i(n+m)[m\bar{\epsilon}_t' - (n+1)\epsilon_g']\delta_{n-1,q}\delta_{mp}}{2n+1} + \frac{i(n-m+1)[m\bar{\epsilon}_t' + n\epsilon_g']\delta_{n+1,q}\delta_{mp}}{2n+1}, \quad \text{(A1c)}$$

$$\overline{o}_{pq}^{mn} = \frac{-i(n+m)(n+1)[m\bar{\epsilon}_t' + (n-1)\epsilon_g']\delta_{n-1,q}\delta_{mp}}{n(n-1)(2n+1)} - \frac{i(n-m+1)n[m\bar{\epsilon}_t' - (n+2)\epsilon_g']\delta_{n+1,q}\delta_{mp}}{(n+1)(n+2)(2n+1)}, \quad \text{(A1d)}$$

$$\overline{p}_{pq}^{mn} = \left\{\frac{[(2n^2+2n+3)m^2 + (2n^2+2n-3)n(n+1)]\bar{\epsilon}_t'}{n(n+1)(2n-1)(2n+3)} + \frac{(4n^2+4n-3)m\epsilon_g'}{n(n+1)(2n-1)(2n+3)}\right\}\delta_{nq}\delta_{mp} + \delta_{nq}\delta_{mp} - \frac{(n+1)(n+m-1)(n+m)\bar{\epsilon}_t'\delta_{n-2,q}\delta_{mp}}{(n-1)(2n-1)(2n+1)} - \frac{n(n-m+1)(n-m+2)\bar{\epsilon}_t'\delta_{n+2,q}\delta_{mp}}{(n+2)(2n+1)(2n+3)}, \quad \text{(A1e)}$$

$$\overline{q}_{pq}^{mn} = +\frac{(n+1)(n+m-1)(n+m)\bar{\epsilon}_t'\delta_{n-2,q}\delta_{mp}}{(2n-1)(2n+1)} - \frac{n(n-m+1)(n-m+2)\bar{\epsilon}_t'\delta_{n+2,q}\delta_{mp}}{(2n+1)(2n+3)} - \frac{(n^2+n-3m^2)\bar{\epsilon}_t' - m(2n-1)(2n+3)\epsilon_g'}{(2n-1)(2n+3)} \times \delta_{nq}\delta_{mp}. \quad \text{(A1f)}$$

By changing $o, p, q, \bar{\epsilon}_t', \epsilon_t', \epsilon_g'$, and mn to $g, e, f, \bar{\mu}_t', \mu_t', \mu_g'$, and uv, respectively, the coefficients of $\tilde{g}_{pq}^{uv}$, $\tilde{e}_{pq}^{uv}$, $\tilde{f}_{pq}^{uv}$, $\overline{g}_{pq}^{uv}$, $\overline{e}_{pq}^{uv}$, and $\overline{f}_{pq}^{uv}$ can be obtained. Detailed derivation of these matrix elements can be found in [31]. For the definition and the orthogonal relations of spherical vector wave functions, readers can refer to [34,35].

[1] L. Saviot, D. B. Murray, E. Duval, A. Mermet, S. Sirotkin, and M. C. Marco de Lucas, Phys. Rev. B **82**, 115450 (2010).
[2] J. Adamek, D. Campo, and J. C. Niemeyer, Phys. Rev. D **82**, 086006 (2010).
[3] D. L. Kovrizhin, Phys. Rev. B **81**, 125130 (2010).
[4] R. Botet and H. Kuratsuji, Phys. Rev. E **81**, 036602 (2010).
[5] A. P. McCauley, A. W. Rodriguez, J. D. Joannopoulos, and S. G. Johnson, Phys. Rev. A **81**, 012119 (2010).
[6] E. Wandersman, V. Dupuis, E. Dubois, and R. Perzynski, Phys. Rev. E **80**, 041504 (2009).
[7] P. Rodriguez-Lopez, S. J. Rahi, and T. Emig, Phys. Rev. A **80**, 022519 (2009).
[8] C.-W. Qiu, A. Novitsky, H. Ma, and S. Qu, Phys. Rev. E **80**, 016604 (2009).
[9] L. Saviot and D. B. Murray, Phys. Rev. B **79**, 214101 (2009).
[10] V. Boţan, F. Pesth, T. Schilling, and M. Oettel, Phys. Rev. E **79**, 061402 (2009).
[11] D. Han, Y. Lai, K. H. Fung, Z.-Q. Zhang, and C. T. Chan, Phys. Rev. B **79**, 195444 (2009).
[12] J. M. Hopkinson and H.-Y. Kee, Phys. Rev. B **79**, 014421 (2009).
[13] T. Stöckli, J.-M. Bonard, A. Châtelain, Z. L. Wang, and P. Stadelmann, Phys. Rev. B **61**, 5751 (2000).
[14] Z.-Y. Li, J. Wang, and B.-Y. Gu, Phys. Rev. B **58**, 3721 (1998).
[15] I. H. H. Zabel and D. Stroud, Phys. Rev. B **48**, 5004 (1993).
[16] Z. Chen and P. Sheng, Phys. Rev. B **39**, 9816 (1989).
[17] R. S. Markiewicz, Phys. Rev. B **18**, 4260 (1978).
[18] A. F. Yagli, Ph.D. thesis, Syracuse University, New York, 2006.
[19] J. N. Damask, *Polarization Optics in Telecommunications*, 1st ed. (Springer, New York, 2004), p. 122.
[20] R. Graglia, P. Uslenghi, and R. Zich, Proc. IEEE **77**, 750 (1989).
[21] V. Varadan, A. Lakhtakia, and V. Varadan, IEEE Trans. Antennas Propag. **AP-37**, 800 (1989).
[22] S. N. Papadakis, N. K. Uzunoglu, and C. N. Capsalis, J. Opt. Soc. Am. A **7**, 1708 (1990).
[23] W. C. Chew, *Waves and Fields in Inhomogeneous Media* (Van Nostrand Reinhold, New York, 1990).
[24] W. Ren, Phys. Rev. E **47**, 664 (1993).

[25] K.-L. Wong and Y.-T. Cheng, IEE Proceedings-H: Microwave, Antennas Propag. **139**, 314 (1992).
[26] L. Gao, T. H. Fung, K. W. Yu, and C. W. Qiu, Phys. Rev. E **78**, 046609 (2008).
[27] Y. L. Geng, X. B. Wu, and L. W. Li, Radio Sci. **38**, 12 (2003).
[28] Y. L. Geng, X. B. Wu, L. W. Li, and B. R. Guan, Phys. Rev. E **70**, 056609 (2004).
[29] Y. L. Geng, X. B. Wu, L. W. Li, and B. R. Guan, IEEE Trans. Antennas Propag. **53**, 3982 (2005).
[30] Y. L. Geng, C. W. Qiu, and N. Yuan, IEEE Trans. Antennas Propag. **57**, 572 (2009).
[31] Z. F. Lin and S. T. Chui, Phys. Rev. E **69**, 056614 (2004).
[32] M. K. Liu, N. Ji, Z. F. Lin, and S. T. Chui, Phys. Rev. E **72**, 056610 (2005).
[33] N. Ji, M. K. Lin, J. Zhou, and Z. F. Lin, Appl. Opt. **13**, 5192 (2005).
[34] S. Y. Liu and Z. F. Lin, Phys. Rev. E **73**, 066609 (2006).
[35] J. L.-W. Li and W. L. Ong, IEEE Trans. Antennas Propag. **59**, 3370 (2011).
[36] S. Liu, L. W. Li, M. S. Leong, and T. S. Yeo, Micro. Opt. Technol. Lett. **25**, 159 (2000).
[37] C. W. Qiu, L. W. Li, Q. Wu, and T. S. Yeo, IEEE Antennas Wireless Propag. Lett. **4**, 467 (2005).
[38] C. W. Qiu, S. Zouhdi, and A. Razek, IEEE Trans. Antennas Propag. **55**, 3515 (2007).
[39] C. W. Qiu, L. W. Li, T. S. Yeo, and S. Zouhdi, Phys. Rev. E **75**, 026609 (2007).
[40] C. W. Qiu and B. Luk'yanchuk, J. Opt. Soc. Am. A **25**, 1623 (2008).
[41] C. W. Qiu, L. Gao, J. D. Joannopoulos, and M. S. Cić, Laser Photon. Rev. (to be published).
[42] X. B. Wu and K. Yasumoto, J. Appl. Phys. **82**, 1996 (1997).
[43] J. C. Monzon, IEEE Trans. Antennas Propag. **37**, 728 (1989).
[44] Y.-l. Xu, J. Opt. Soc. Am. A **20**, 2093 (2003).
[45] Y.-l. Xu, Phys. Rev. E **67**, 046620 (2003).
[46] C. F. Bohren and D. R. Huffman, *Absorption and Scattering of Light by Small Particles* (Wiley, New York, 1983).
[47] W. J. Wiscombe, Appl. Opt. **19**, 1505 (1980).
[48] L. Tsang, J. A. Kong, and R. T. Shin, *Theory of Microwave Remote Sensing* (Wiley-Interscience, New York, 1985).
[49] B. Stout, M. Nevière, and E. Popov, J. Opt. Soc. Am. A **24**, 1120 (2006).
[50] J. A. Stratton, *Electromagnetic Theory* (McGraw-Hill, New York, 1941).
[51] L. Tsang and J. A. Kong, *Scattering of Electromagnetic Waves: Theories and Applications* (Wiley-Interscience, New York, 2000).
[52] Y.-l. Xu, Appl. Opt. **36**, 9496 (1997).
[53] Y. L. Geng and S. He, J. Zhejiang Univ. Sci. A **7**, 99 (2006).